

Emergence of Gapless Quantum Spin Liquid from Deconfined Quantum Critical Point

Wen-Yuan Liu¹, Juraj Hasik², Shou-Shu Gong³, Didier Poilblanc², Wei-Qiang Chen^{4,5,*} and Zheng-Cheng Gu^{1,†}


¹*Department of Physics, The Chinese University of Hong Kong, Shatin, New Territories, Hong Kong, China*

²*Laboratoire de Physique Théorique, C.N.R.S. and Université de Toulouse, 31062 Toulouse, France*

³*Department of Physics and Peng Huanwu Collaborative Centre for Research and Education, Beihang University, Beijing 100191, China*

⁴*Shenzhen Key Laboratory of Advanced Quantum Functional Materials and Devices, Southern University of Science and Technology, Shenzhen 518055, China*

⁵*Shenzhen Institute for Quantum Science and Engineering and Department of Physics, Southern University of Science and Technology, Shenzhen 518055, China*

 (Received 9 March 2022; revised 16 August 2022; accepted 17 August 2022; published 19 September 2022)

Quantum spin liquids (QSLs) as novel phases of matter with long-range entanglement and deconfined quantum critical points (DQCPs) as descriptions for unconventional phase transitions between two ordered states beyond the standard paradigm, such as the transition between antiferromagnetic (AFM) and valence-bond solid (VBS) phases, are two representative emerging phenomena. These implications for understanding correlated materials and developing theoretical frameworks for many-body physics are of crucial importance. Here, we show that a gapless QSL can naturally emerge from a DQCP. Via large-scale tensor network simulations of a square-lattice spin-1/2 frustrated Heisenberg model, both QSL-state and DQCP-type AFM-VBS transitions are observed. By tuning the coupling constants, the AFM-VBS transition vanishes, and instead, a gapless QSL phase gradually develops in between. Remarkably, along the phase boundaries of AFM-QSL and QSL-VBS transitions, we always observe the same correlation-length exponents, $\nu \approx 1.0$, which is intrinsically different from the one of the DQCP-type transition, indicating new types of universality classes. Our results explicitly demonstrate a new scenario for understanding the emergence of gapless QSL from an underlying DQCP. The discovered QSL phase survives in a large region of tuning parameters, and we expect its experimental realization in solid-state materials or quantum simulators.

DOI: [10.1103/PhysRevX.12.031039](https://doi.org/10.1103/PhysRevX.12.031039)

Subject Areas: Condensed Matter Physics, Magnetism, Strongly Correlated Materials

I. INTRODUCTION

At low temperature, quantum fluctuations can melt magnetic orders in condensed matter systems, leading to the emergence of new phases of quantum matter and unconventional quantum phase transitions. A prominent example is the quantum spin liquid (QSL), which preserves both spin rotation symmetry and lattice symmetry. QSL states can exhibit collective phenomena such as emergent gauge fields and fractional excitations, which are qualitatively different from an ordinary paramagnet [1]. In the past several decades, QSL has attracted numerous attention

since it was proposed as the parent state of high-temperature cuprate superconductors [2]. Nowadays, there are ongoing efforts searching for QSL due to its exotic topological properties.

Another well-known example is the zero-temperature continuous phase transition between an antiferromagnetic (AFM) state and a valence-bond solid (VBS) state, which cannot be understood by the standard Landau-Ginzburg-Wilson (LGW) paradigm. To describe such a continuous phase transition between two ordered phases, a deconfined quantum critical point (DQCP) scenario was proposed, where fractional excitations and an emergent gauge field also naturally arise [3,4]. In the DQCP theory, the fundamental degrees of freedom are fractionalized spinon excitations with spin 1/2. The condensation of spinons leads to the AFM phase while the confinement of spinons leads to the VBS phase. Right at the critical point, the deconfined spinons couple to the emergent $U(1)$ gauge field, and enhanced symmetries have been observed numerically [5–7].

*chenwq@sustech.edu.cn

†zcg@phy.cuhk.edu.hk

Published by the American Physical Society under the terms of the [Creative Commons Attribution 4.0 International license](https://creativecommons.org/licenses/by/4.0/). Further distribution of this work must maintain attribution to the author(s) and the published article's title, journal citation, and DOI.

Previously, the DQCP-related physics has been extensively studied in sign-problem-free models [5–24]. In most cases, the obtained physical quantities exhibit unusual scaling violations, and it is unclear whether the observed phase transition between AFM and VBS states is continuous or weakly first order. The reason for these perplexing phenomena remains an enigma, and different scenarios have been proposed for explanations [19,25–35]. According to Anderson, a QSL state can be regarded as a resonating valence bond (RVB) state or the superposition of different kinds of VBS patterns, and the translational symmetry is restored by quantum fluctuations. In fact, DQCP can also be regarded as a special kind of unstable RVB state from which both VBS order and AFM order are developed. While QSL and DQCP are mostly studied separately, in very few cases they might be observed in the same system, and thus it is a mystery whether the two concepts have any intrinsic relation [35,36].

In this work, we present a specific example where both gapless QSL and DQCP can be observed in a single frustrated model. The gapless QSL gradually develops from the DQCP by tuning parameters. To the best of our knowledge, this is the first concrete example to explicitly show the possible intrinsic relation between DQCP and QSL. Such a relation can provide crucial insights into the understanding of the underlying physics of DQCP and the gapless QSL phase. In particular, we investigate a spin-1/2 square-lattice model, which contains first-, second-, and third-nearest neighbor Heisenberg exchange interaction couplings J_1 , J_2 , and J_3 , respectively, described by the following Hamiltonian:

$$H = J_1 \sum_{\langle i,j \rangle} \mathbf{S}_i \cdot \mathbf{S}_j + J_2 \sum_{\langle\langle i,j \rangle\rangle} \mathbf{S}_i \cdot \mathbf{S}_j + J_3 \sum_{\langle\langle\langle i,j \rangle\rangle\rangle} \mathbf{S}_i \cdot \mathbf{S}_j. \quad (1)$$

We set $J_1 = 1$, and the couplings J_2 , J_3 are tuning parameters. This model gained much interest in the early days after high-temperature superconductivity was discovered. Although there are analytic and small-size numerical results [37–48], its phase diagram is still far from clear, especially for the region with strong quantum fluctuations. By using the state-of-the-art tensor network method, both DQCP and gapless QSL are observed around this region. The phase diagram summarizing these results is shown in Fig. 1. Remarkably, along the phase boundaries of AFM-QSL and QSL-VBS transitions, we always observe the same correlation-length exponents, $\nu \approx 1.0$. In contrast, along the phase boundary of the AFM-VBS transition, we observe that the correlation-length exponents are intrinsically close to the one from other DQCP studies based on similar sizes, which is $\nu \approx 0.8$ [5]. These findings reveal the deep relations between DQCP and QSL, and provide us with invaluable guidance for understanding the gapless QSL developed from an underlying DQCP as well as the experimental realization of gapless QSL in square-lattice-based materials or quantum simulators.

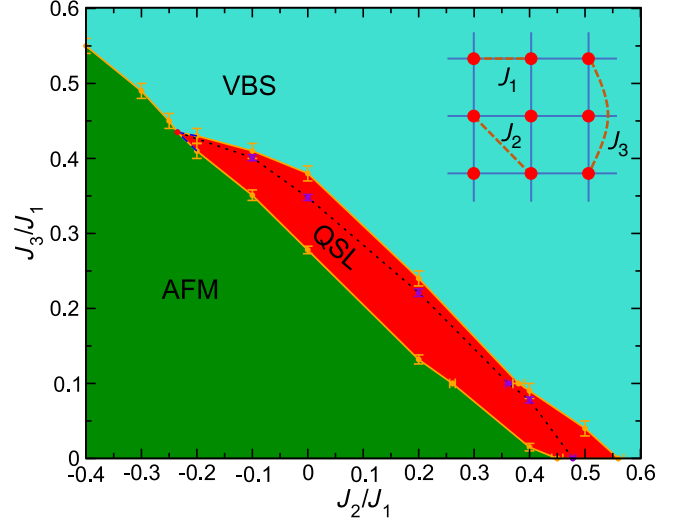


FIG. 1. Ground-state phase diagram of the J_1 - J_2 - J_3 model, including three phases: the AFM, VBS, and gapless QSL (red region) phases. The blue dashed line denotes the unknown shape of the QSL phase close to the tricritical point. Violet points on the black dotted line in the QSL phase have the same decay power for spin and dimer correlations. Error bars denote 1 standard deviation.

II. CONTINUOUS AFM-TO-VBS TRANSITION

We first consider the phase diagram of the J_1 - J_2 - J_3 model in the region with a fixed significant ferromagnetic J_2 coupling, e.g., $J_2 = -0.4$, $J_2 = -0.3$, or $J_2 = -0.25$. In this situation, J_2 coupling will enhance the AFM order, coordinating with the J_1 coupling. With an increasing AFM coupling J_3 , we observe a direct transition from the AFM to the VBS phase. The (squared) AFM order parameter $\langle \mathbf{M}_0^2 \rangle$ is defined as the value of the structure factor $S(\mathbf{k}) = (1/L^2) \sum_{ij} \langle \mathbf{S}_i \cdot \mathbf{S}_j \rangle e^{i\mathbf{k} \cdot (\mathbf{i}-\mathbf{j})}$ at the wave vector $\mathbf{k}_0 = (\pi, \pi)$, i.e., $\langle \mathbf{M}_0^2 \rangle = (1/L^2) S(\mathbf{k}_0)$. In Fig. 2(a), we present the AFM order (squared) on different $L \times L$ systems up to 20×20 . Finite-size scaling reveals the disappearance of the AFM order at $J_3 = J_{c1} \approx 0.55$, for $J_2 = -0.4$.

Then, we measure the dimer order parameter (DOP) to detect the possible spontaneous appearance of a VBS order. The DOP on open boundary conditions is defined as [36,49]

$$D_\alpha = \frac{1}{N_b} \sum_{\mathbf{i}} (-1)^{i_\alpha} B_{\mathbf{i}}^\alpha, \quad (2)$$

where $B_{\mathbf{i}}^\alpha = \mathbf{S}_{\mathbf{i}} \cdot \mathbf{S}_{\mathbf{i}+e_\alpha}$ is the bond operator between site \mathbf{i} and site $\mathbf{i} + e_\alpha$ along the α direction with $\alpha = x$ or y , and $N_b = L(L-1)$ is the corresponding total number of counted bonds along the α direction. The horizontal DOP $\langle D_x^2 \rangle$ based on the bond-bond correlations is presented in Fig. 2(c) with the largest size up to 20×20 . One can see that the DOP vanishes in the 2D limit at $J_3 = 0.54$

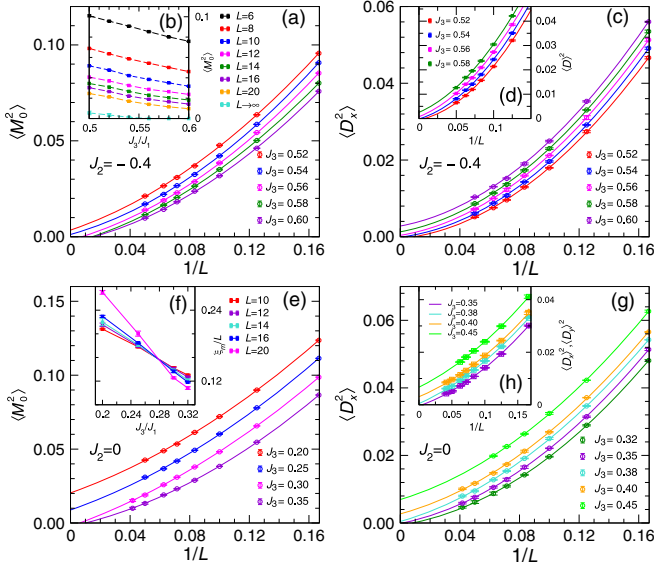


FIG. 2. Scaling analysis of (squared) order parameters of the J_1 - J_2 - J_3 model at $J_2 = -0.4$ (a)–(d) and at $J_2 = 0$ (e)–(h). (a,e) Finite-size scaling of AFM order parameters. (b) J_3 dependence of AFM orders on different sizes. (c,g) Horizontal dimer order parameters $\langle D_x^2 \rangle$ based on bond-bond correlations. (d) Boundary-induced dimer order parameters $\langle D \rangle^2$. (f) Dimensionless quantity ξ_m/L . (h) Boundary-induced dimer order parameters along both the x direction ($\langle D_x \rangle^2$, square symbols) and the y direction ($\langle D_y \rangle^2$, diamond symbols). All extrapolations with respect to $1/L$ are performed through second-order polynomial fits. Error bars denote 1 standard deviation of the sampled mean values.

but acquires a nonzero extrapolated value at $J_3 = 0.56$ indicating a VBS order. As a double-check, boundary-induced dimerizations $\langle D \rangle^2 = \langle D_x \rangle^2 + \langle D_y \rangle^2$ are also shown in Fig. 2(d), which also suggests that VBS order sets in just above $J_3 = J_{c2} \simeq 0.55$. Our analysis then shows that $J_{c2} \simeq J_{c1}$, giving strong evidence for a direct AFM-VBS transition point, located at $J_3 \simeq 0.55$ for $J_2 = -0.4$. As shown in Fig. 2(b), the AFM order parameter on each size shows a smooth variation with respect to J_3 . Therefore, based on our results, the AFM-VBS transition is very likely to be continuous, though the possibility of a weak first-order transition cannot be completely ruled out.

III. EMERGENT QSL PHASE

Next, we set $J_2 = 0$; i.e., we investigate the phase diagram of the J_1 - J_3 model. Through a finite-size scaling analysis shown in Fig. 2(e), we can see that the AFM order still survives at $J_3 = 0.25$ but vanishes at $J_3 = 0.3$ in the thermodynamic limit. To determine the phase transition point precisely and conveniently, a dimensionless quantity ξ_m/L is computed, where ξ_m is the correlation length defined as $\xi_m = (L/2\pi)\sqrt{[S(\pi, \pi)/S(\pi, \pi + 2\pi/L)] - 1}$ [50], which clearly shows that the AFM phase transition point is located at $J_3 = J_{c1} \simeq 0.28$ in Fig. 2(f).

We then measure dimer order parameters to detect possible VBS order. The horizontal DOP $\langle D_x^2 \rangle$ is presented in Fig. 2(c) with the largest size up to 24×24 . One can see that the DOP in the 2D limit is close to zero at $J_3 = 0.38$ but appears at $J_3 = 0.40$ with an obvious nonzero extrapolated value characterizing a VBS order. In addition, the boundary-induced dimerizations $\langle D_x \rangle^2$ and $\langle D_y \rangle^2$ shown in Fig. 2(d) also suggest the absence of VBS order for $J_3 \lesssim 0.38$. Note that the extrapolated values of $\langle D_x^2 \rangle$ and $\langle D_x \rangle^2$ are 0.0004(4) and 0.0004(3) at $J_2 = 0.38$; 0.0027(5) and 0.0031(4) at $J_3 = 0.40$; 0.0069(6) and 0.0067(4) at $J_3 = 0.45$, respectively, very consistent with each other in all three cases (for all $L \times L$ sizes presented here, the x and y directions are isotropic with $\langle D_x \rangle^2 = \langle D_y \rangle^2$). These results demonstrate the reliability of our calculations. Therefore, by excluding spin and dimer orders, a QSL phase is suggested for $0.28 \lesssim J_3 \lesssim 0.38$. We note that a recent study using other methods suggests a QSL phase for $0.3 \lesssim J_3 \lesssim 0.375$ [51], which is very close to our results.

Now, we turn to the $J_2 > 0$ case, in which J_1 , J_2 , and J_3 couplings compete with each other. To complete the full phase diagram of the J_1 - J_2 - J_3 model, we compute the relevant order parameters along two vertical lines, $J_2 = 0.2$ and $J_2 = 0.4$, varying J_3 (see Appendix B 3), as well as along a horizontal line $J_3 = 0.1$ varying J_2 . Through a finite-size scaling analysis of the order parameters, we locate the QSL phase in the regions $0.13 \lesssim J_3 \lesssim 0.24$ along the line $J_2 = 0.2$, $0.015 \lesssim J_3 \lesssim 0.09$ along the line $J_2 = 0.4$, and $0.26 \lesssim J_2 \lesssim 0.38$ along the line $J_3 = 0.1$, sandwiched by the AFM and VBS phases.

To confirm the existence of a potential QSL phase, we further compare the finite-size projected entangled pair state (PEPS) results with infinite PEPS (iPEPS) results at two typical points $(J_2, J_3) = (0, 0.35)$ and $(0.2, 0.2)$, which we find to be inside the QSL phase from our finite PEPS calculations. At these two points, the thermodynamic-limit ground-state energies from finite-size scaling are $-0.56995(9)$ and $-0.53982(9)$, in very good agreement with the corresponding iPEPS ground-state energies $-0.56956(2)$ and $-0.53966(2)$. Furthermore, by measuring order parameters, the iPEPS results also support the idea that the two points are in the QSL phase. More details can be seen in Appendix C. Thus, our results strongly indicate a QSL phase in the J_1 - J_2 - J_3 model in an extended region of the two-dimensional tuning parameter space (J_2, J_3) . Finite-size effects have been effectively reduced by a detailed comparison of systems of increasing size up to 24×24 , backed up by supplementary iPEPS computations directly in the thermodynamic limit.

Finally, we focus on the strip between the vertical line $J_2 = -0.3$, hosting a direct AFM-VBS transition at $J_3 \simeq 0.49$ and another vertical line $J_2 = 0$ with a wide QSL phase for $0.28 \lesssim J_3 \lesssim 0.38$. By analyzing order parameters, at fixed $J_2 = -0.25$, a direct AFM-VBS transition occurs at $J_3 \simeq 0.45$, and at fixed $J_2 = -0.2$, the QSL potentially

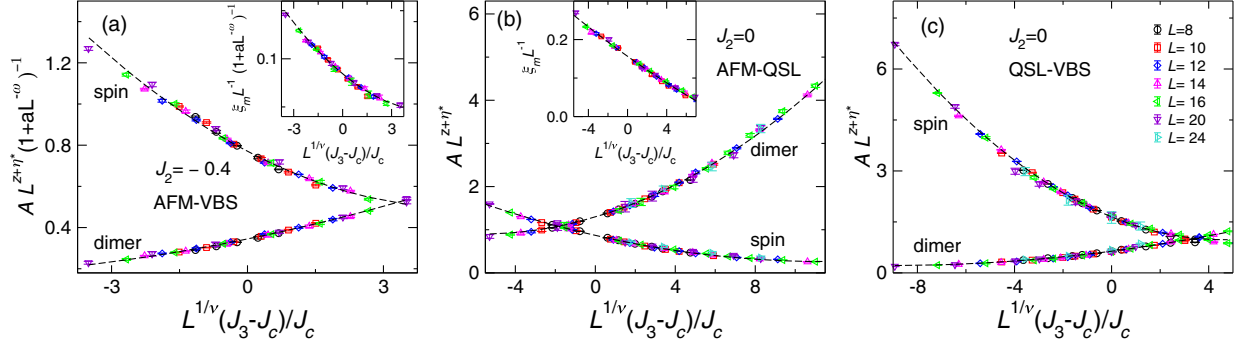


FIG. 3. Scaling of physical quantities including order parameters and correlation lengths. (a) At the AFM-VBS transition point with a fixed $J_2 = -0.4$, using $\nu = 0.82$, $J_c = 0.55$, $z + \eta_s^* = 1.33$, $z + \eta_d^* = 1.36$, and $\omega = 1.5$. Prefactors a are 11.5, 3.8, 11.3 for the quantity ξ_m , $\langle M_0^2 \rangle$, and $\langle D_x^2 \rangle$, correspondingly. (b) At the AFM-QSL transition point with a fixed $J_2 = 0$, using $\nu = 1.02$, $J_c = 0.278$, $z + \eta_s^* = 1.21$, and $z + \eta_d^* = 1.89$. (c) At the QSL-VBS transition point with a fixed $J_2 = 0$, using $\nu = 1.02$, $J_c = 0.38$, $z + \eta_s^* = 1.69$, and $z + \eta_d^* = 1.40$. For AMF-QSL and QSL-VBS transitions, subleading corrections are not used. Black dashed lines are quadratic curves using the corresponding critical exponents.

appears in a small region $0.41 \lesssim J_3 \lesssim 0.43$ and evidently expands to a relatively large region $0.35 \lesssim J_3 \lesssim 0.41$ at fixed $J_2 = -0.1$ (see Appendix B 3). This reveals how the QSL can gradually emerge by increasing the J_2 coupling from the DQCP, which describes the continuous transition line between the AFM and VBS phases.

IV. CRITICAL EXPONENTS

To extract critical exponents for the quantum phase transitions between QSL and AFM/VBS phases, we analyze the scaling of physical quantities according to the standard scaling formula with a possible subleading correction [5,50]:

$$A(J_3, L) = L^\kappa (1 + aL^{-\omega}) F[L^{1/\nu} (J_3 - J_c) / J_c], \quad (3)$$

where $A = \xi_m$, $\langle M_0^2 \rangle$, or $\langle D_x^2 \rangle$, and $\kappa = 1$ for ξ_m , $-(z + \eta_s^*)$ for $\langle M_0^2 \rangle$, and $-(z + \eta_d^*)$ for $\langle D_x^2 \rangle$, in which η_s^* and η_d^* are corresponding spin and dimer correlation function exponents and z is the dynamic exponent at the transition. Factors a and ω are tuning parameters of the subleading term. Here, J_3 is the tuning parameter with a fixed J_2 .

We first consider the quantities scaling for the AFM-VBS transition with fixed $J_2 = -0.4$. The transition point is estimated at $J_3 \simeq 0.55$ from a finite-size scaling analysis of order parameters as mentioned previously, and it is actually also supported by the crossing of the dimensionless quantity ξ_m/L . To achieve a good data collapse for these quantities, we find a subleading correction is necessary. As seen in the inset of Fig. 3(a), the spin correlation length ξ_m at different sizes and couplings can be scaled using $\nu = 0.82(5)$ and $J_c = 0.55(1)$. Next, we keep ν and J_c fixed to extract spin and dimer correlation function exponents, which leads to $z + \eta_s^* = 1.33(6)$ and $z + \eta_d^* = 1.36(5)$. In these cases, a subleading term has been used with fixed $\omega = 1.5$ and different a for ξ_m , $\langle M_0^2 \rangle$,

and $\langle D_x^2 \rangle$, respectively. Note that the obtained critical exponents including ν , $z + \eta_s^*$, and $z + \eta_d^*$ are close to those from the $J-Q$ model based on the similar system sizes.

Now, we consider the critical exponents for the AFM-QSL transition at J_{c1} and the QSL-VBS transition at J_{c2} . In this case, we find that a single correlation-length exponent ν can scale the physical quantities very well at the two transition points, as shown in Figs. 3(b) and 3(c) for the data collapse of the $J_1 - J_3$ model, i.e., at fixed $J_2 = 0$. We also choose other fixed values including $J_2 = -0.1, 0.2$, and 0.4 with the tuning parameter J_3 , as well as fixed $J_3 = 0.1$ with the tuning parameter J_2 , to extract critical exponents at their transition points, and they have the same behavior. In these cases, a good data collapse can be obtained without subleading correction terms. The critical exponents are listed in Table I.

From Table I, we can see that, for all cases of the AFM-QSL and QSL-VBS transitions at a fixed J_2 or J_3 , the corresponding spin and dimer correlation exponents $z + \eta_s^*$ and $z + \eta_d^*$ are consistent for each kind of transition. Roughly, $z + \eta_{s1}^* \sim 1.2$ and $z + \eta_{d1}^* \sim 1.9$ for the AFM-QSL transition, and $z + \eta_{s2}^* \sim 1.6$ and $z + \eta_{d2}^* \sim 1.5$ for the QSL-VBS transition. The correlation exponents for the $J_1 - J_2$ model (i.e., for fixed $J_3 = 0$) show slight differences, probably caused by a very large correlation length. In this case, the density matrix renormalization group (DMRG) results have not yet converged well even with as many as $M = 14000$ SU(2) kept states [equivalent to about 56000 U(1) states] on 12×28 strips [36], unlike the $J_1 - J_2 - J_3$ model for which $M = 10000$ works very well for two typical points $(J_2, J_3) = (0, 0.35)$ and $(0.2, 0.2)$ that are also in the QSL phase (see Appendix B 1). Most importantly, all of these cases support the same correlation-length exponent, i.e., $\nu \approx 1.0$. In particular, $\nu \approx 1$ is apparently different from that of the AFM-VBS transition obtained in the $J-Q$ model or in the

TABLE I. Critical exponents of the J_1 - J_2 - J_3 model at the AFM-QSL and QSL-VBS transition points using fixed J_2 or J_3 , or at the AFM-VBS transition using fixed $J_2 = -0.25, -0.3$, and -0.4 . Note that $J_3 = 0$ results are taken from Ref. [36]. Results of the J - Q model up to 32×32 [5] are listed for comparison. Numbers in brackets are 1 standard deviation. Errors of the critical point J_c are estimated from finite-size scaling analysis of order parameters or fitting correlation lengths. Values of ν for QSL-related transitions are an average of several values from fitting order parameters at the transition points (see Appendix B 4). Spin and dimer exponents $z + \eta^*$ are obtained by data collapse using the listed values of ν and J_c .

Model	Type	$z + \eta_s^*$	$z + \eta_d^*$	ν	J_c
$J-Q$	AFM-VBS	1.26(3)	1.26(3)	0.78(3)	
$J_2 = -0.4$	AFM-VBS	1.33(6)	1.36(5)	0.82(5)	0.55(1)
$J_2 = -0.3$	AFM-VBS	1.35(3)	1.32(4)	0.86(6)	0.49(1)
$J_2 = -0.25$	AFM-VBS	1.31(3)	1.34(3)	0.89(5)	0.45(1)
$J_2 = -0.1$	AFM-QSL	1.31(1)	1.83(1)	1.03(6)	0.351(7)
$J_2 = -0.1$	QSL-VBS	1.60(1)	1.53(1)	1.03(6)	0.41(1)
$J_2 = 0$	AFM-QSL	1.21(1)	1.89(2)	1.02(5)	0.278(5)
$J_2 = 0$	QSL-VBS	1.69(2)	1.40(2)	1.02(5)	0.38(1)
$J_2 = 0.2$	AFM-QSL	1.18(1)	1.95(1)	1.01(4)	0.132(6)
$J_2 = 0.2$	QSL-VBS	1.63(3)	1.45(3)	1.01(4)	0.24(1)
$J_2 = 0.4$	AFM-QSL	1.31(1)	1.88(1)	1.04(3)	0.015(5)
$J_2 = 0.4$	QSL-VBS	1.63(1)	1.51(2)	1.04(3)	0.09(1)
$J_3 = 0.1$	AFM-QSL	1.17(2)	1.93(1)	1.00(7)	0.261(5)
$J_3 = 0.1$	QSL-VBS	1.60(1)	1.54(1)	1.00(7)	0.38(1)
$J_3 = 0$	AFM-QSL	1.38(3)	1.72(4)	0.99(6)	0.45(1)
$J_3 = 0$	QSL-VBS	1.96(4)	1.26(3)	0.99(6)	0.56(1)

$J_1 - J_2 - J_3$ model with similar system sizes. These features strongly suggest new universality classes for the AFM-QSL and QSL-VBS transitions.

V. CORRELATION FUNCTIONS IN THE QSL PHASE

To understand the physical nature of the QSL phase, we measure spin-spin and dimer-dimer correlation functions along the central row on a 12×28 strip where both x and y directions are open. Specifically, we first look at spin correlations at different J_3 with fixed $J_2 = 0$, as shown in Fig. 4(a). In the AFM phase, spin correlations at $J_3 = 0$ and 0.25 decay very slowly and tend to saturate at long distances. In the VBS phase, spin correlations at $J_3 = 0.45$ and 0.5 have a clear exponential decay behavior, though some oscillations appear due to the mixture of short-range spiral orders, which will be discussed elsewhere. Compared with these two cases, the spin correlations at $J_3 = 0.35$, which are in the QSL phase, exhibit a long tail, indicating a

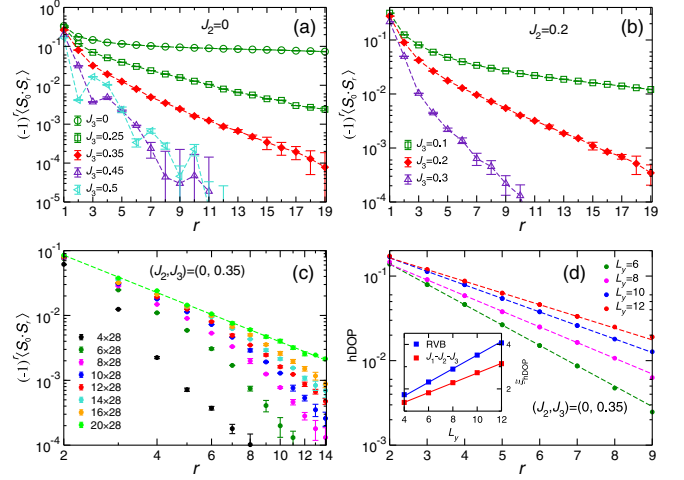


FIG. 4. Decay behavior of correlations. We show spin correlation functions of the J_1 - J_2 - J_3 model with a fixed $J_2 = 0$ (a) and a fixed $J_2 = 0.2$ (b), on a 12×28 strip along the central row at different J_3 . (c) Fixing $L_x = 28$, the variation of spin correlations on strip $L_y \times L_x$ with L_y increasing from 4 to 20 at a typical point $(J_2, J_3) = (0, 0.35)$ in the QSL phase. The green dashed line denotes the power-law fit $y = cr^{-\alpha_s}$ for $L_y = 20$. (d) At $(J_2, J_3) = (0, 0.35)$, the log-linear plot of hDOP obtained on different $L_y \times 28$ with respect to the distance from the left edge along the central line. Corresponding decay lengths for different L_y are extracted from exponential fits (shown as straight dashed lines). The inset shows a clear linear growth of the hDOP decay length for the gapless RVB spin-liquid state (blue) and the QSL state at $(J_2, J_3) = (0, 0.35)$ (red), with L_y increasing with slopes 0.301(4) and 0.219(2), respectively. Error bars denote 1 standard deviation of the sampled mean values.

likely power-law decay behavior. Similarly, for the given $J_2 = 0.2$, which has a QSL phase in the region $0.13 \lesssim J_3 \lesssim 0.24$, spin correlations at $J_3 = 0.1, 0.2$, and 0.3 show three different kinds of decay behavior, corresponding to the AFM, QSL, and VBS phases, shown in Fig. 4(b). Focusing on the two typical points in the QSL phase, $(J_2, J_3) = (0, 0.35)$ and $(0.2, 0.2)$, we make detailed comparisons with the results from the DMRG method based on a 12×28 strip. The PEPS energy, spin, and dimer correlation functions all agree excellently with those of the converged DMRG results; see Appendix B 1.

To provide more evidence to show the decay behavior of correlations in the QSL phase, taking $(J_2, J_3) = (0, 0.35)$ as an example, we consider how they change on different system sizes. In Fig. 4(c), we present the spin correlations on different L_y from 4 to 20. By fixing $L_x = 28$, we expect that their behavior would approach the real 2D one when increasing L_y . Increasing L_y from 10 to 20, we can see that the long-distance correlations increase significantly, tending to a power-law decay behavior, and the power exponent is $\alpha_s \simeq 1.91(2)$ from $L_y = 20$ correlations.

Then, we detect the dimer behavior by using the characteristic decay length of the local horizontal dimer

order parameter (hDOP) for a given L_y . The hDOP is defined as the difference ΔB between nearest strong and weak horizontal bond energies,

$$\Delta B(r) = |B_r^x - B_{r+e_x}^x|. \quad (4)$$

The hDOP decays exponentially from the left system boundary, and the corresponding decay length ξ_{hDOP} can be extracted, shown in Fig. 4(d) at $(J_2, J_3) = (0, 0.35)$. We find that the decay length ξ_{hDOP} grows linearly with increasing system size L_y , consistent with a power-law decay behavior of the dimer-dimer correlation functions in the QSL phase. Actually, the same behavior of ξ_{hDOP} has already been observed in a short-range RVB state, whose dimer correlations decay in a power law, as well as in the gapless QSL phase in the $J_1 - J_2$ model ($J_3 = 0$) [36]. Note that here $L_x = 28$ is long enough to extract the correct ξ_{hDOP} for L_y ranging from 4 to 12, while for larger L_y , a relatively large L_x is necessary to minimize finite-size effects on ξ_{hDOP} , which has also been observed in the calculations of the RVB state [36]. In summary, these results suggest that the discovered QSL is gapless with power-law decay behaviors of both spin and dimer correlations.

VI. DISCUSSION

In summary, by applying the state-of-the-art tensor network method, we study the phase diagram of the spin-1/2 J_1 - J_2 - J_3 square-lattice AFM model. For negative and large J_2 , we find strong evidence for a direct, continuous, AFM-VBS Landau-forbidden transition line. Along this critical line, exponents are close to those obtained in the $J - Q$ model [5,12] or in classical cubic-lattice dimer models [7,11], suggesting the same universality class described by DQCP. In particular, spin and dimer correlations decay with similar exponents, indicating an emergent SO(5) symmetry that rotates the AFM and the VBS order parameters into each other [6,7]. Whether this symmetry is exact or approximate needs further investigation. Surprisingly, we also found that the AFM-VBS transition line ends at—what could be—a tricritical point, from which a gapless QSL arises and forms an extended critical phase, separating the AFM and VBS phases. Remarkably, both AFM-QSL and QSL-VBS phase transitions have the same correlation-length exponents $\nu \approx 1.0$, indicating new types of universality classes.

We stress that the gapless QSL found here is very different from the gapless U(1) deconfined phase obtained by the compact quantum electrodynamics with fermionic matter on square lattices, including correlation behaviors and critical exponents [52,53]. A recent SU(2) gauge theory [54] based on a fermionic parton construction [55] proposed a gapless \mathbb{Z}_2 spin liquid as a candidate for such an intermediate phase. However, variational Monte Carlo (VMC) simulations of the corresponding Gutzwiller-projected ansatz [56] found constant correlation-function

exponents $z + \eta_s \sim z + \eta_d \sim 2$, in contrast to our findings (see Appendix B 3) showing smaller, varying exponents. Moreover, the SU(2) gauge theory further predicts a weak breaking of SO(5) symmetry for the AFM-QSL phase transition, which is very different from our results in Fig. 1, where the line with $z + \eta_s = z + \eta_d \sim 1.55$ [consistent with the potential SO(5) symmetry] is rather far away from the AFM-QSL phase boundary. In addition, we also note that a tricritical point does not naturally emerge from such a gauge theory, which first resorts to a first-order transition to connect the AFM-VBS critical line to the QSL phase, and we have detected no sign of first-order behavior in our simulations.

As both QSL and DQCP are associated with gauge fluctuations and fractionalized spinon excitations, the underlying field theory for QSL may have a close relation to the DQCP theory [3,4]. The possibility of an emergent topological theta term from the DQCP is a very promising future direction [36]. Experimentally, the large region of QSL can be sought for based on square-lattice materials, and quantum simulators are also a promising platform to realize the novel phase diagram discovered here [57–59].

ACKNOWLEDGMENTS

We thank Anders Sandvik for useful comments. This work was supported by the NSFC/RGC Joint Research Scheme No. N-CUHK427/18, the ANR/RGC Joint Research Scheme No. A-CUHK402/18 from Hong Kong's Research Grants Council No. 11861161001 from the National Natural Science Foundation of China, and the TNSTRONG ANR-16-CE30-0025 and TNTOP ANR-18-CE30-0026-01 grants awarded by the French Research Council. S. S. G. was supported by the National Natural Science Foundation of China Grants No. 11874078 and No. 11834014, and the Fundamental Research Funds for the Central Universities. W. Q. C. was supported by the Science, Technology and Innovation Commission of Shenzhen Municipality (No. ZDSYS20190902092905285), the Guangdong Basic and Applied Basic Research Foundation under Grant No. 2020B1515120100, and the Shenzhen-Hong Kong Cooperation Zone for Technology and Innovation (Grant No. HZQB-KCZYB-2020050). This work was also granted access to the HPC resources of the CALMIP Supercomputing Center under Allocation No. 2017-P1231 and the Center for Computational Science and Engineering at Southern University of Science and Technology.

APPENDIX A: TENSOR NETWORK METHODS

Tensor network states provide a powerful and efficient representation to encode low-energy physics based on their local entanglement structure, whose representation accuracy is systematically controlled by the bond dimension D of the tensors [60]. As a numerical approach, tensor

network states are very suitable to simulate frustrated magnets, where quantum Monte Carlo methods fail. The tensor network state methods we used include the finite-size PEPS, the iPEPS, and the DMRG methods. The DMRG is a well-established method to simulate 1D and quasi-1D systems, and here, SU(2) spin rotation symmetries are incorporated to improve the accuracy [61].

For the finite PEPS algorithm, we use open boundary conditions and each tensor is independent. The finite PEPS ansatz allows us to simulate uniform and nonuniform phases with incommensurate short-range or long-range spiral orders. In our calculations, the finite PEPS works in the scheme of variational Monte Carlo sampling, and the summation of physical freedoms is replaced by the Monte Carlo sampling [62–65]. The physical quantities are evaluated by important sampling according to the weights of given spin configurations, which can be effectively obtained by contracting single-layer tensor networks. When optimizing the PEPS, we first perform the simple update imaginary-time evolution method for initializations [66] and then use the stochastic gradient method for accurate optimization to obtain the ground states [62,63]. With the obtained ground states, physical quantities—including energies, correlations functions, and order parameters—are computed via Monte Carlo sampling. More details can be found in Ref. [63]. Unless otherwise specified, we use $D = 8$ for finite PEPS calculations, which is good enough to obtain convergent results (see Appendix B). When computing spin and dimer correlations on the central line of the lattice, we use about 60 000 000 Monte Carlo sweeps, which can have a standard deviation of the mean about 1×10^{-4} or smaller for each value at different distances. When computing order parameters that contain all kinds of correlations, we usually use 1 000 000 Monte Carlo sweeps, which produce 1 standard deviation of the mean about 2×10^{-4} on a 20×20 square lattice, and it takes about 3 days using 500 Intel(R) Xeon(R) E5-2690 v3 CPU cores for such a calculation after the optimization process. This work took about 10 million CPU hours.

The iPEPS method is widely used to directly simulate infinite two-dimensional systems, which have translation invariance. The iPEPS used here only has a single unique tensor, which can describe the antiferromagnetic phase and the uniform paramagnetic phase. The largest bond dimension we used is $D = 8$, and the thermodynamic properties can be evaluated with appropriate extrapolations with respect to the bond dimension or the corresponding correlation length.

APPENDIX B: FINITE PEPS RESULTS

1. Comparison with DMRG

We compare finite PEPS results with those from the DMRG method with SU(2) spin rotation symmetry. Based on the $J_1 - J_2$ model, it has been shown that finite PEPS

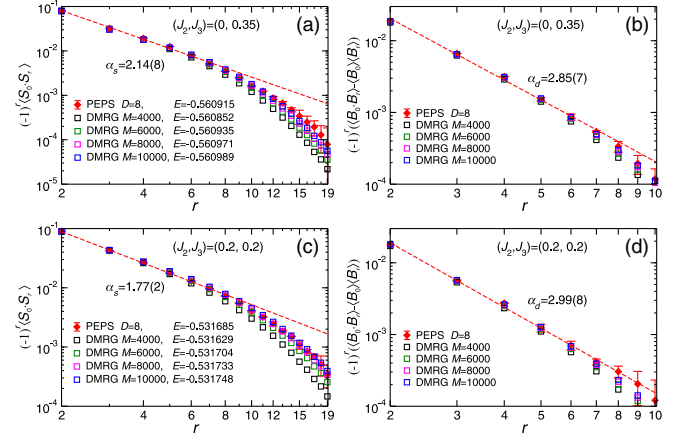


FIG. 5. Correlation functions of the J_1 - J_2 - J_3 model on a 12×28 strip along the central line. (a,b) Spin and dimer correlations at $(J_2, J_3) = (0, 0.35)$ and (c,d) those at $(J_2, J_3) = (0.2, 0.2)$. Red dashed lines denote power-law fits $y = cr^{-\alpha}$ for the correlation values with $r \leq 7$, and corresponding exponents α_s (α_d) for the spin (dimer) are presented.

results agree very well with the convergent DMRG results in our previous work [36,63]. For the $J_1 - J_3$ model discussed here, the squared AFM order $\langle \mathbf{M}_0^2 \rangle$ at $J_3/J_1 = 0.3$ calculated by PEPS is 0.09 865 on the 6×6 lattice and 0.06 568 on the 8×8 lattice on open boundary conditions, also in excellent agreement with those calculated by DMRG on the same systems, which are 0.09 886 and 0.06 588, correspondingly. Now, we consider larger sizes on the $J_1 - J_2 - J_3$ model. Figures 5(a) and 5(c) depict the spin correlations at the two points $(J_2, J_3) = (0, 0.35)$ and $(0.2, 0.2)$ in the QSL phase. DMRG results with different numbers of SU(2) kept state are presented up to $M = 10000$ [equivalent to about 40 000 U(1) states]. The corresponding ground-state energies for different M are listed with each legend showing that DMRG and PEPS energies are highly consistent. When increasing M , the DMRG spin correlations gradually increase until convergence, which is also in excellent agreement with PEPS results. The connected dimer-dimer correlations along the x direction in the QSL phase, defined as

$$C_d(r) = \langle B_0^x B_r^x \rangle - \langle B_0^x \rangle \langle B_r^x \rangle, \quad (\text{B1})$$

are also computed, as shown in Figs. 5(d). We can see that the PEPS and DMRG dimer-dimer correlations also agree very well. Note that such agreements are consistent with our previous results for the pure $J_1 - J_2$ model, i.e., $J_3 = 0$. In the pure $J_1 - J_2$ model, DMRG needs a very large bond dimension M to converge spin correlations, at least up to $M = 12000$ at $J_2/J_1 = 0.5$ and more than $M = 14000$ [equivalent to about 56 000 U(1) states] at $J_2/J_1 = 0.55$, but a $D = 8$ PEPS can produce convergent results quite well compared to the $D = 10$ PEPS results [36]. However, for the two points $(J_2, J_3) = (0, 0.35)$ and $(0.2, 0.2)$ we

discuss here, DMRG with $M = 10000$ already obtains well-converged correlations, indicating that the results already converge at $D = 8$ PEPS.

2. Convergence of finite PEPS with bond dimension

To check the D -convergence behavior, we consider the spin and dimer correlations based on large sizes, including 16×28 and 20×28 sites, using $D = 4, 6, 8$, and 10 . We choose the point $(J_2, J_3) = (0, 0.35)$, which is critical and belongs to the most challenging for accurate simulations. For each case, we use the simple update imaginary-time evolution method for initialization; we then use the stochastic gradient method for further optimization. From Fig. 6, we can see that, after increasing $D = 4$ to $D = 8$, the energy, spin, and dimer correlations all have significant improvement. However, after increasing $D = 8$ to $D = 10$, the improvement is very small, indicating that the results already converge at $D = 8$. Since the size 20×28 is among the largest ones in the finite-size simulations and $(J_2, J_3) = (0, 0.35)$ is critical, the above results suggest that at $D = 8$, the presented results for other finite sizes at different values of J_2 and J_3 can also converge. Actually, in our previous studies, we have demonstrated that at $D = 8$, the results can converge well for the Heisenberg model up to 32×32 sites and the frustrated $J_1 - J_2$ model up to 24×24 sites [36,63]. Unless otherwise specified, $D = 8$ is used for finite PEPS calculations.

3. Gapless QSL region

We consider the J_1 - J_2 - J_3 model with a fixed $J_2 > 0$. Here, we take $J_2 = 0.2$ and $J_2 = 0.4$ as examples. We first focus on the $J_2 = 0.2$ case. AFM and VBS order parameters, as well as the correlation length ξ_m of the spin

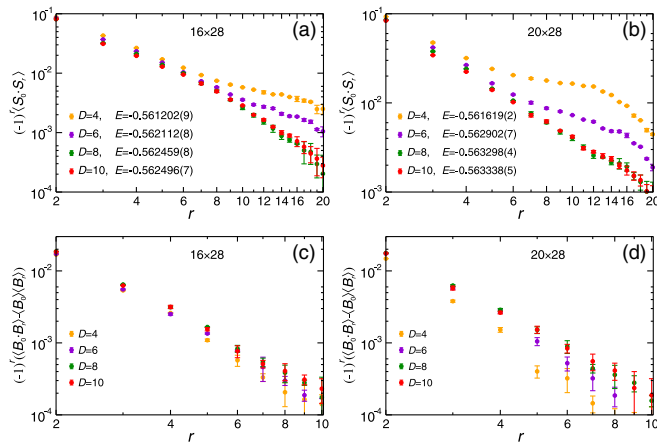


FIG. 6. Convergence of finite PEPS calculations with respect to bond dimension D at $(J_2, J_3) = (0, 0.35)$. (a,b) Spin correlation functions of the J_1 - J_2 - J_3 model on 16×28 and 20×28 strips along the central line. (c,d) Corresponding dimer-dimer correlations. Energies using different D are listed in the legend.

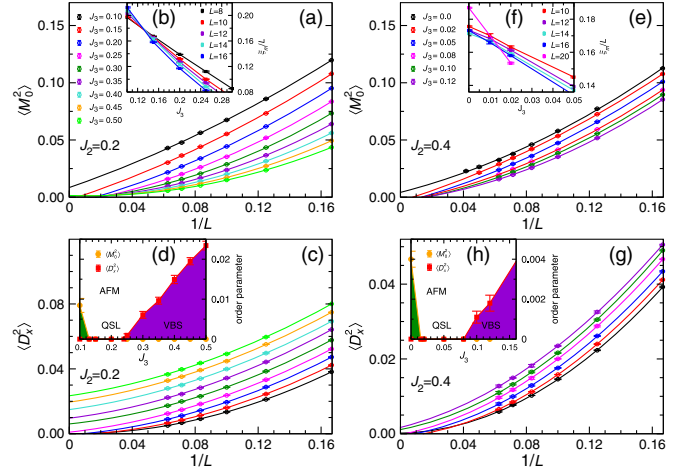


FIG. 7. (a)–(d) Order parameters and phase diagrams for $J_2 = 0.2$ and (e)–(h) $J_2 = 0.4$. (a,c) AFM and VBS order parameters at $J_2 = 0.2$, respectively, with the same legend symbols. (b) Dimensionless quantity ξ_m/L at $J_2 = 0.2$ for different system sizes. (d) Phase diagram at $J_2 = 0.2$, including AFM, (gapless) QSL, and VBS phases. (e)–(h) Corresponding diagrams at $J_2 = 0.4$. All extrapolations are quadratic fits.

structure factor, are shown in Figs. 7(a)–7(d). From Fig. 7(a), one can find that the AFM order vanishes between $J_3 = 0.1$ and $J_3 = 0.15$; in fact, the behavior of ξ_m/L shows that the AFM-QSL transition point is estimated at $J_3 \simeq 0.13$. Meanwhile, from a finite-size scaling analysis, the VBS order starts to appear at $J_3 \simeq 0.24$, as presented in Fig. 7(c). Thus, given $J_2 = 0.2$, in the region

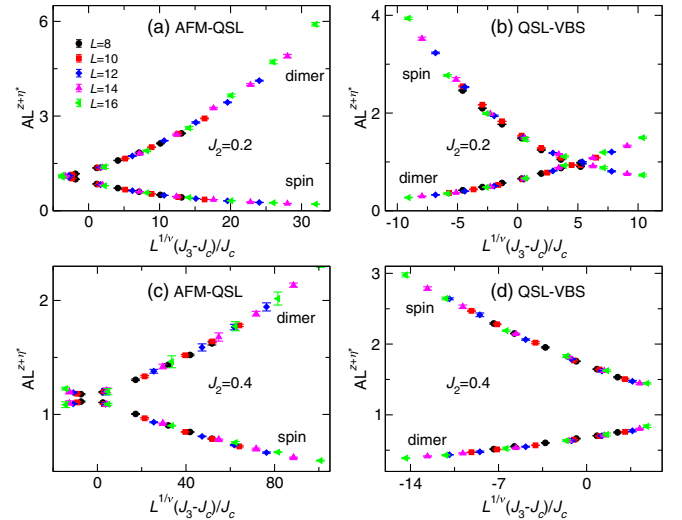


FIG. 8. Data collapse of spin and dimer orders for AFM-QSL and QSL-VBS phase transition points at fixed $J_2 = 0.2$ (a,b) and $J_2 = 0.4$ (c,d). Scaling at the AFM-QSL transition point $J_{c1} = 0.132$ (a) and the QSL-VBS transition point $J_{c2} = 0.24$ (b) along $J_2 = 0.2$ with $\nu = 1.01$. Scaling at the AFM-QSL transition point $J'_{c1} = 0.015$ (c) and the QSL-VBS transition point $J'_{c2} = 0.09$ (d) along $J_2 = 0.4$ with $\nu = 1.04$.

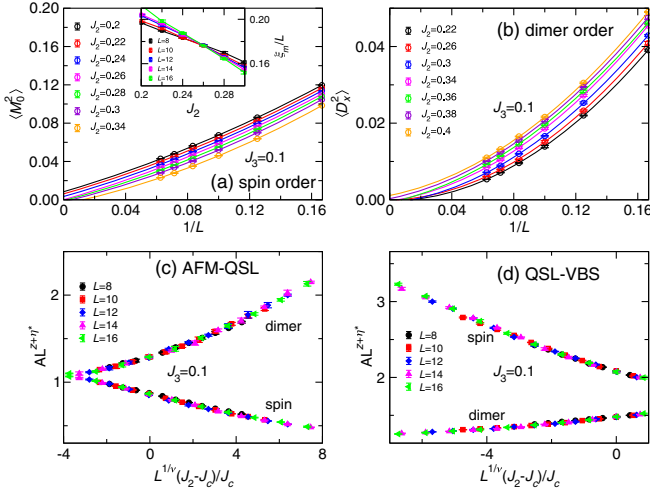


FIG. 9. Given $J_3 = 0.1$, order parameters at different J_2 . Finite-size scaling of spin (a) and dimer (b) order parameters through second-order extrapolations. The inset of panel (a) shows the crossing of the dimensionless quantity ξ_m/L . Data collapse of spin and dimer orders at the AFM-QSL transition point $J_{c1} = 0.261$ (c) and the QSL-VBS transition point $J_{c2} = 0.38$ (d), with $\nu = 1.00$.

$0.13 \lesssim J_3 \lesssim 0.24$, it is a QSL phase. A similar analysis is applied to $J_2 = 0.4$, and a QSL phase in the region $0.015 \lesssim J_3 \lesssim 0.09$ is also discovered, as shown in Figs. 7(e)–7(h). Note that the dimer structure factor on open boundary systems is not well defined [36,49], so in this context, we cannot use the dimer correlation lengths based on dimer structure factors to locate the onset of VBS orders. The data collapse for extracting critical exponents is shown in Fig. 8.

Similarly, we can also explore the phase diagram by sweeping J_2 with a fixed J_3 . We use $J_3 = 0.1$ as an example. As shown in Fig. 9, we compute the spin and dimer order parameters at different J_2 ranging from $J_2 = 0.2$ to 0.4 . In Figs. 9(a) and 9(b), one can clearly see that the AFM order vanishes at $J_2 \simeq 0.26$, and the VBS order begins to appear for $J_2 > 0.38$. Thus, for the region $0.26 \lesssim J_2 \lesssim 0.38$, it is a QSL phase. Here, we note that $(J_2, J_3) = (0.38, 0.1)$ is located at the QSL-VBS phase boundary, compatible with previous calculations along the vertical line $J_2 = 0.4$, where $(J_2, J_3) = (0.4, 0.1)$ is in the VBS phase.

We also consider ferromagnetic J_2 couplings. Using $J_2 = -0.1$, a QSL in the region $0.35 \lesssim J_3/J_1 \lesssim 0.41$ is suggested, sandwiched by the AFM phase and the VBS phase, shown in Fig. 10. With a stronger $J_2 = -0.2$, the QSL phase further shrinks to a very narrow region $0.41 \lesssim J_3/J_1 \lesssim 0.43$. Further enhancing $J_2 = -0.25$ ($J_2 = -0.3$), a continuous AFM-VBS transition is suggested at $J_3 \simeq 0.45$ ($J_3 \simeq 0.49$), with the QSL phase disappearing. The scaling analyses are shown in Figs. 11 and 12. Actually, for the three cases with fixed $J_2 = -0.2$, -0.25 , and -0.3 and for regions of J_3 close to the tricritical point, we compute the VBS order parameters with two

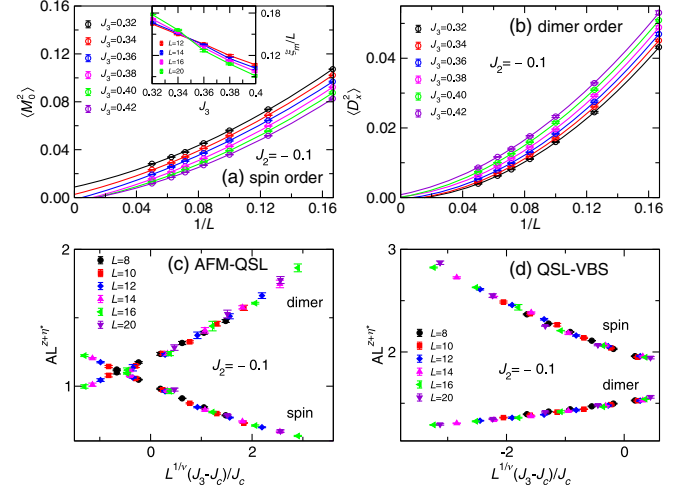


FIG. 10. Given $J_2 = -0.1$, order parameters at different J_3 . Finite-size scaling of spin (a) and dimer (b) order parameters through second-order extrapolations. The inset of panel (a) shows the crossing of the dimensionless quantity ξ_m/L . Data collapse of spin and dimer orders at the AFM-QSL transition point $J_{c1} = 0.351$ (c) and the QSL-VBS transition point $J_{c2} = 0.41$ (d), with $\nu = 1.03$.

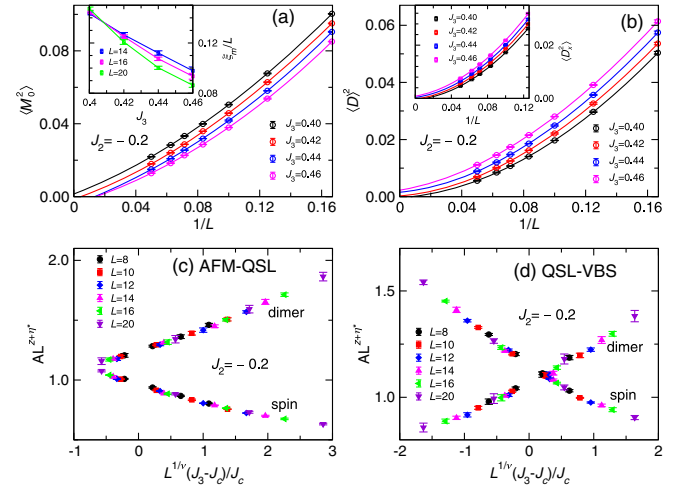


FIG. 11. Scaling of quantities at given $J_2 = -0.2$. (a,b) AFM and boundary-induced dimer order parameters $\langle D \rangle^2 = \langle D_x \rangle^2 + \langle D_y \rangle^2$ with cubic fits for $L = 6$ –20. The inset of panel (a) shows the crossing of the dimensionless quantity ξ_m/L , and the inset of panel (b) shows the dimer order parameter defined based on bond-bond correlations $\langle D_x^2 \rangle$ with quadratic fits for $L = 8$ –20. (c,d) Data collapse at the AFM-QSL and QSL-VBS transition points $J_{c1} = 0.41$ and $J_{c2} = 0.43$, respectively. At AFM-QSL transitions $J_{c1} = 0.41$, the quantities can collapse using $z + \eta_{d1}^* = 1.31(4)$, $z + \eta_{d1}^* = 1.84(4)$ and $\nu = 0.95(8)$. At QSL-VBS transitions $J_{c2} = 0.43$, the quantities can be collapsed using $z + \eta_{d2}^* = 1.42(3)$, $z + \eta_{d2}^* = 1.74(5)$, and $\nu = 0.95(8)$.

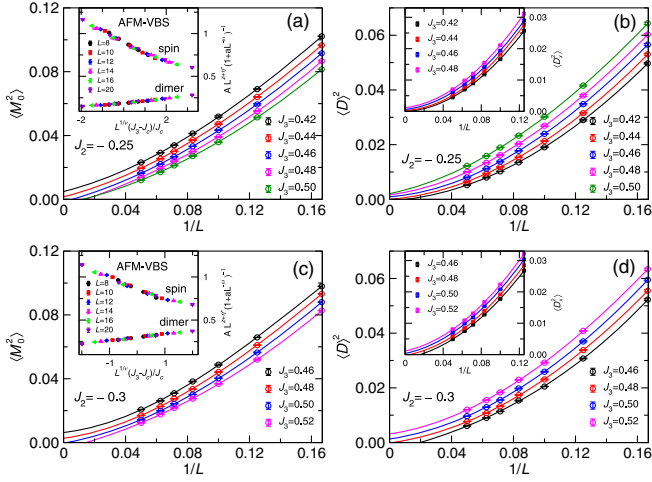


FIG. 12. Scaling of quantities at given $J_2 = -0.25$ (a,b) and $J_2 = -0.3$ (c,d). (a,b) AFM and dimer order parameters $\langle D \rangle^2$ at $J_2 = -0.25$ with cubic fits for $L = 6-20$. The inset of panel (b) shows $\langle D_x^2 \rangle$ with quadratic fits for $L = 8-20$. The inset of panel (a) shows the data collapse at the AFM-VBS transition point using $J_c = 0.45$, $\nu = 0.89$, $z + \eta_s^* = 1.31$ with subleading factors $a = 2.2$ and $\omega = 1.9$, and $z + \eta_d^* = 1.34$ with subleading factors $a = 9.5$ and $\omega = 0.9$. (c,d) AFM and dimer order parameters $\langle D \rangle^2$ at $J_2 = -0.3$ with cubic fits for $L = 6-20$. The inset of panel (d) shows $\langle D_x^2 \rangle$ with quadratic fits for $L = 8-20$. The inset of panel (c) shows the data collapse at the AFM-VBS transition point using $J_c = 0.49$, $\nu = 0.86$, $z + \eta_s^* = 1.35$ with subleading factors $a = 3$ and $\omega = 1.5$, and $z + \eta_d^* = 1.32$ with subleading factors $a = 12$ and $\omega = 1.5$.

definitions $\langle D \rangle^2 = \langle D_x \rangle^2 + \langle D_y \rangle^2$ and $\langle D_x \rangle^2$, and we carefully check the finite-size scaling versus $1/L$ using different fitting functions and different sizes. The onset of VBS order is estimated at $J_3 = 0.43(1)$, $J_3 = 0.45(1)$, and $J_3 = 0.49(1)$, respectively.

In the gapless QSL region, we can extract the spin and dimer decay powers $z + \eta_{s,d}$ according to a scaling $A \propto L^{-(z+\eta)}$. As seen in Fig. 13, for a fixed J_2 or J_3 , the extracted spin (dimer) power decreases (increases) with increasing J_3 or J_2 . Such a characteristic is not supportable for a gapless \mathbb{Z}_2 QSL, which has a constant decay power in the whole QSL region, according to the VMC simulations of the corresponding Gutwiller-projected ansatz [56]. An interesting feature for the cases in Fig. 13 is that

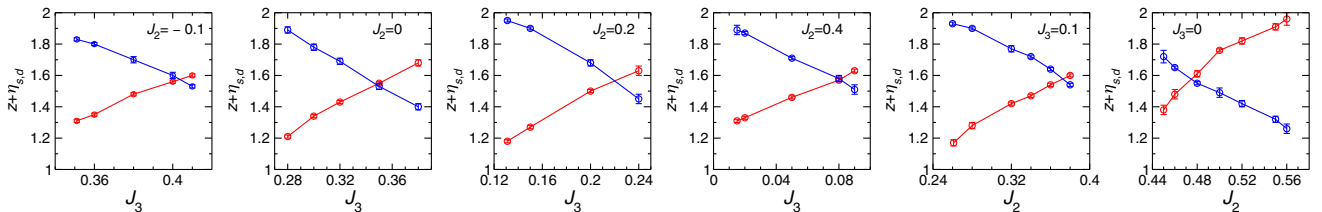


FIG. 13. Exponent $z + \eta_{s,d}$ for the spin (red) and dimer (blue) at different couplings at fixed J_2 or J_3 , in the QSL phase, computed from order parameter A according to the scaling $A \propto L^{-(z+\eta)}$.

$z + \eta_s$ and $z + \eta_d$ always have a crossing at a value around 1.55. A reasonable speculation is that an $\text{SO}(5)$ symmetry emerges at these crossing points. Thus, we guess that there exists a line for different (J_2, J_3) in the whole QSL region, on which it has $\text{SO}(5)$ symmetry. Note that in the calculations at $J_2 = -0.2$, where the QSL region is very narrow $0.41 \lesssim J_3 \lesssim 0.43$, very close to the tricritical point, crossing of the spin and dimer decay power in the QSL phase does not occur (see the values in the caption of Fig. 11), which might be caused by finite-size effects.

4. Extracting critical exponents

Accurately determining critical exponents in a numerical way is very challenging for unconventional 2D phase transitions, which often can only be realized in unbiased simulations like quantum Monte Carlo computations [6,8,19], and the accuracy depends on system sizes and sampling errors. In our tensor network results, the precision of physical quantities may also have some influence, but we still try to evaluate the reasonability of critical exponents, especially focusing on the correlation-length exponent ν_1 at the AFM-QSL transition and ν_2 at the QSL-VBS transition, which we claim to be the same. The physical quantities from different sizes and different couplings are collectively fitted for collapse, according to the formula [5,50]

$$A(J_3, L) = L^\kappa (1 + aL^{-\omega}) F[L^{1/\nu}(J_3 - J_c)/J_c], \quad (\text{B2})$$

where $A = \xi_m$, $\langle M_0^2 \rangle$, or $\langle D_x^2 \rangle$, and $\kappa = 1$ for ξ_m , $-(z + \eta_s^*)$ for $\langle M_0^2 \rangle$, and $-(z + \eta_d^*)$ for $\langle D_x^2 \rangle$. Factors a and ω are tuning parameters of the subleading term. Note that $F[\]$ is a polynomial function, and here, a second-order expansion is used, considering our largest system size is 24×24 (a third-order fitting is also tested and has a negligible third-order coefficient). Usually, the subleading term is not included for fitting of the AFM-QSL and QSL-VBS transitions. The transition point J_c can be estimated from the scaling analysis of order parameters or the spin correlation length, which is mostly used as a fixed value for fitting critical exponents.

We take the $J_1 - J_3$ model, i.e., $J_2 = 0$, as an example. The AFM-QSL transition occurs at $J_{c1} = J_3 \approx 0.28$. It can also be given from a collective fit of J_{c1} and ν_1 , which gives the critical point $J_{c1} = 0.278(5)$ and the correlation-length

TABLE II. Critical exponents obtained by a collective fitting of ν and $z + \eta^*$ using a fixed critical point. In each fit, ν and $z + \eta^*$ are free parameters. Fitting AFM order parameters gives $\nu_{1,s}$ and $z + \eta_{s1}^*$ at the AFM-QSL critical point, and it gives $\nu_{2,s}$ and $z + \eta_{s2}^*$ at the QSL-VBS critical point. Fitting VBS order parameters gives $\nu_{1,d}$ and $z + \eta_{d1}^*$ at the AFM-QSL critical point, and it gives $\nu_{2,d}$ and $z + \eta_{d2}^*$ at the QSL-VBS critical point. Errors are from fittings. The last column $\bar{\nu}$ is an average over $\nu_{1,s}$, $\nu_{1,d}$, $\nu_{2,s}$, and $\nu_{2,d}$. The last row represents the averaged values of $z + \eta$ over different J_2 or J_3 .

	$\nu_{1,s}$	$\nu_{1,d}$	$\nu_{2,s}$	$\nu_{2,d}$	$\bar{\nu}$
$J_2 = -0.1$	0.96(6)	1.01(7)	1.09(5)	1.04(1)	1.03(6)
$J_2 = 0$	1.10(3)	0.98(6)	1.05(4)	0.96(5)	1.02(5)
$J_2 = 0.2$	1.04(3)	0.94(4)	1.14(6)	0.93(3)	1.01(4)
$J_2 = 0.4$	1.09(4)	0.96(3)	1.11(2)	0.99(4)	1.04(3)
$J_3 = 0.1$	1.06(9)	1.03(4)	0.96(6)	0.95(8)	1.00(7)
	$z + \eta_{s1}^*$	$z + \eta_{d1}^*$	$z + \eta_{s2}^*$	$z + \eta_{d2}^*$	
$J_2 = -0.1$	1.28(2)	1.82(1)	1.61(1)	1.53(2)	
$J_2 = 0$	1.17(2)	1.87(5)	1.67(3)	1.44(2)	
$J_2 = 0.2$	1.17(2)	1.99(2)	1.65(2)	1.49(2)	
$J_2 = 0.4$	1.28(1)	1.87(1)	1.62(1)	1.49(1)	
$J_3 = 0.1$	1.18(2)	1.93(2)	1.62(2)	1.52(2)	
Average	1.22(2)	1.90(2)	1.63(2)	1.49(2)	

exponent 1.01(9). Using a fixed $J_{c1} = 0.278$, we can evaluate the correlation-length exponent ν_1 independently from AFM and VBS order parameters, respectively, by a collective fit of ν and $z + \eta^*$. Fitting AFM order gives $\nu_{1,s} = 1.10(3)$ and $z + \eta_{s1}^* = 1.17(2)$, and fitting VBS order gives $\nu_{1,d} = 0.98(6)$ and $z + \eta_{d1}^* = 1.87(5)$. The three fits produce consistent ν_1 . At the QSL-VBS transition, the critical point is located at $J_{c2} = 0.38(1)$ according to the finite-size scaling of VBS order parameters. In this case, we cannot use a similar correlation length defined based on the dimer structure factor to locate the transition point since the dimer structure factor on open boundary systems is not well defined [36,49]. However, we can still check ν_2 from the fitting of AFM and VBS order parameters by using a fixed $J_{c2} = 0.38$. The AFM order fit gives $\nu_{2,s} = 1.05(4)$ and $z + \eta_{s2}^* = 1.67(3)$, and the VBS order fit gives $\nu_{2,d} = 0.96(5)$ and $z + \eta_{d2}^* = 1.44(2)$. The two fits also give consistent ν_2 (assuming other J_{c2} like $J_{c2} = 0.37$ for fitting gives almost the same ν_2). Note the obtained ν_1 at the AFM-QSL transition point and ν_2 at the QSL-VBS transition point indicate $\nu_1 \approx \nu_2 \approx 1.0$.

Similar analyses are applied to other cases for a fixed J_2 or a fixed J_3 . By scaling AFM and VBS order parameters with fixed critical points, collective fits of two parameters ν and $z + \eta^*$ can give $\nu_{1,s}$, $\nu_{1,d}$, $\nu_{2,s}$, and $\nu_{2,d}$, respectively, associated with their corresponding $z + \eta_{s1}^*$, $z + \eta_{d1}^*$, $z + \eta_{s2}^*$, and $z + \eta_{d2}^*$, as listed in Table II. Remarkably, the obtained ν all agree well, close to 1.0, indicating the same correlation-length exponent ν at the AFM-QSL and QSL-VBS transitions. Meanwhile, the fitted spin and dimer

TABLE III. Critical exponents obtained by using a single correlation-length exponent $\bar{\nu}$ at the AFM-QSL and QSL-VBS transition points. In each fit, $z + \eta^*$ is a free parameter, and $\bar{\nu}$ is fixed. Errors are from fittings.

	$z + \eta_{s1}^*$	$z + \eta_{d1}^*$	$z + \eta_{s2}^*$	$z + \eta_{d2}^*$	$\bar{\nu}$
$J_2 = -0.1$	1.31(2)	1.83(1)	1.60(1)	1.53(1)	1.03
$J_2 = 0$	1.21(1)	1.89(2)	1.69(2)	1.40(2)	1.02
$J_2 = 0.2$	1.18(1)	1.95(1)	1.63(3)	1.45(3)	1.01
$J_2 = 0.4$	1.31(1)	1.88(1)	1.63(1)	1.51(2)	1.04
$J_3 = 0.1$	1.17(2)	1.93(1)	1.60(1)	1.54(1)	1.00

critical exponents using different fixed J_2 or J_3 are consistent, respectively, at the AFM-QSL and QSL-VBS transition points. Their rough estimated values are $z + \eta_{s1}^* \sim 1.2$, $z + \eta_{d1}^* \sim 1.9$, $z + \eta_{s2}^* \sim 1.6$, and $z + \eta_{d2}^* \sim 1.5$, as shown in the last row of Table II. In order to clearly show a single correlation-length exponent ν can scale all the physical quantities well for each case, we use the averaged value $\bar{\nu}$ over $\nu_{1,s}$, $\nu_{1,d}$, $\nu_{2,s}$, and $\nu_{2,d}$ as a fixed parameter to fit $z + \eta^*$. The scaled quantities using $\bar{\nu}$ for data collapse are shown in the figures in Appendix B 3, and the fitted values $z + \eta^*$ are listed in Table I in the main text. They are also listed in Table III for a convenient comparison with Table II, which shows small differences in the two tables. This indicates that a single ν close to 1.0 indeed works well at the AFM-QSL and QSL-VBS transitions.

Finally, let us discuss the χ^2 (per degree of freedom) of the fittings, which quantifies the goodness of a fit. Usually, $\chi^2 \sim 1.0$ or smaller means a satisfactory fit. In our optimal fittings, for some cases we indeed have $\chi^2 \sim 1.0$, including the fits at the AFM-VBS transition using $J_2 = -0.4$. But there are some fits with $\chi^2 \sim 3.0$, which is relatively too large for the number of degrees of freedom of the fit. As we know, χ^2 depends on the sampling errors and the data window to fit [50]. For our tensor network results, the obtained physical quantities have slight unavoidable deviations from their exact values due to imperfect optimizations, which also leads to extra influence on the values of χ^2 . This is different from unbiased quantum Monte Carlo simulations where there are no wave-function optimization problems. However, our fits can still give reasonable and correct information to understand the unconventional quantum phase transition, as evidenced by a series of rather smooth curves formed by the scaled quantities with similar critical exponents, at different fixed J_2 or J_3 (as is shown in the previous figures in Appendix B 3), which is just the requirement of the well-behaved universal scaling functions.

APPENDIX C: iPEPS RESULTS

1. Scaling analysis

For iPEPS, resorting to translation symmetry, a single tensor with $U(1)$ and C_{4v} symmetries can be used to

describe the AFM and QSL phases [67]. With different bond dimension D of iPEPS, one can extract the corresponding correlation length and then use the finite- D scaling or the so-called finite correlation-length scaling (FCLS) to obtain the extrapolated physical quantities. Such an approach has been demonstrated to work well on the Heisenberg model (reviewed later). Next, we consider two typical points $(J_2, J_3) = (0, 0.35)$ and $(0.2, 0.2)$ for comparison. In that case, we show that the simple finite correlation-length scaling has to be extended, including simultaneous $1/D$ corrections.

The wave function is completely parametrized by a single, real, rank-5 tensor a , with physical index s for spin-1/2 degrees of freedom and four auxiliary indices u, l, d, r of bond dimension D corresponding to the four directions up, left, right, and down of the square lattice. The tensor a is given by a linear combination $a = \sum_i \lambda_i t_i$ of elementary tensors t , which are distinct representatives of the fully symmetric (A_1) irrep of the C_{4v} point group. The t tensors also obey $U(1)$ charge conservation, i.e., certain assignment of charges \vec{u} to the physical index s and \vec{v} to each of the four auxiliary indices, for some fixed N . For each considered bond dimension, we choose charges $[\vec{u}, \vec{v}] = [u_\uparrow, u_\downarrow, v_0, \dots, v_{D-1}]$, listed in Table IV, based on the analysis of optimal states from the unrestricted simulations of the Néel phase of the $J_1 - J_2$ model [67]. The only variational parameters of this ansatz are the coefficients $\vec{\lambda}$ associated with the family of elementary tensors t .

Observables are evaluated by the corner transfer matrix technique. The optimization of energy per site $e(\vec{\lambda})$ is carried out using the L-BFGS optimizer, which is a gradient-based quasi-Newton method. The gradients of the energy with respect to the parameters $\vec{\lambda}$ are evaluated by reverse-mode automatic differentiation, which differentiates the entire corner transfer matrix procedure, the construction of the reduced density matrices, and finally, the evaluation of spin-spin interactions $\mathbf{S} \cdot \mathbf{S}$ for nearest-neighbor, next-nearest neighbor, and next-next-nearest-neighbor terms. The antiferromagnetic order is incorporated into this translationally invariant wave function by rotation of the physical space on each sublattice-B

site: $\mathbf{S} \cdot \mathbf{S} \rightarrow \mathbf{S} \cdot \tilde{\mathbf{S}}$ with $\tilde{S}^\alpha = -\sigma_y S^\alpha (\sigma_y)^T$. We typically perform gradient optimization until the difference in the energy between two consecutive gradient steps becomes smaller than 10^{-8} . The entire implementation of the ansatz and its optimization are available as part of the open-source library *peps-torch* [68].

a. AFM Heisenberg point $(J_2, J_3) = (0, 0)$

The AFM Heisenberg model, realized at the point $(J_2, J_3) = (0, 0)$, provides a solid benchmark for extrapolation techniques of finite- (D, χ) iPEPS data (note, here, that χ is the cutoff bond dimension of the contracted tensor network). The recently developed finite correlation-length scaling [69,70] coupled with gradient optimization considerably improved upon initial thermodynamic estimates of order parameter m^2 based on the plain $1/D$ scaling. The finite- χ estimate of the correlation length ξ can be readily extracted from the leading part of the spectrum of the transfer matrix as $\xi = -1/\log |\Lambda_1/\Lambda_0|$, where Λ_0 and Λ_1 are the leading and subleading eigenvalues, respectively. In most recent variation of FCLS [71], each (D, χ) optimization was treated as an individual data point. For sufficiently large correlation lengths, the data for the order parameter are expected to obey simple scaling hypothesis ansatz:

$$m^2 = m_0^2 + a/\xi + O(1/\xi^2), \quad (\text{C1})$$

inspired by the established finite-size corrections of the nonlinear $O(3)$ sigma model.

Using the above scaling hypothesis, we analyze the data from iPEPS simulations for $D = (5, 6, 7, 8)$ and select χ from 17 up to 200 for $D = (5, 6, 7)$ and up to 147 for $D = 8$, restricting to states with correlation lengths $1/\xi < 0.3$. This results in an estimate $m^2(1/\xi \rightarrow 0) = 0.0949(2)$, which is very close to the best QMC estimate $m_{\text{QMC}}^2 = 0.09451(2)$. Here, we improve upon this estimate by recognizing that the way magnetization scales with ξ might possess a slight D dependence that vanishes for $D \gg 1$. The extended scaling hypothesis reads

$$m^2 = m_0^2 + a/\xi + b/(D\xi) + O(1/\xi^2). \quad (\text{C2})$$

Fitting this surface to the same data via a nonlinear least-squares fit leads to $m^2(1/D \rightarrow 0, 1/\xi \rightarrow 0) = 0.0947(2)$, which is in better agreement with QMC. We show the fixed- D cuts of the resulting surface (C2) and the comparison of different thermodynamic estimates in Fig. 14.

b. $J_1 - J_3$ model at $(J_2, J_3) = (0, 0.35)$

The optimizations at this highly frustrated point become considerably more demanding. In particular, for bond dimensions $D = (6, 7, 8)$, we observe that the necessary environment dimension for regular behavior of

TABLE IV. The $U(1)$ charges for the Néel phase taking $N = 1$. Charges for $D = 8$ are a prediction. The last column shows the number of elementary tensors t_i .

D	$[u_\uparrow, u_\downarrow, v_0, v_1, \dots, v_{D-1}]$	Number of tensors
2	$[1, -1, 0, 2]$	2
3	$[1, -1, 0, 2, 0]$	12
4	$[1, -1, 0, 2, -2, 0]$	25
5	$[1, -1, 0, 2, -2, 0, 2]$	52
6	$[1, -1, 0, 2, -2, 0, 2, -2]$	93
7	$[1, -1, 0, 2, -2, 0, 2, -2, 2]$	165
8	$[1, -1, 0, 2, -2, 0, 2, -2, 0, 2]$	294

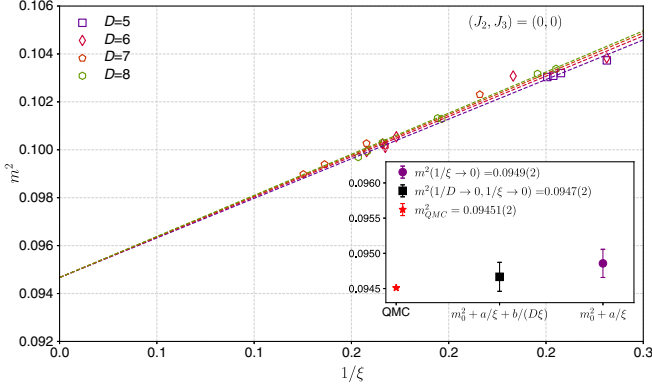


FIG. 14. FCLS of magnetization for the AFM Heisenberg model. Dashed lines represent fixed D cuts of the surface $m^2 = m_0^2 + a/\xi + b/(D\xi)$. The inset shows a comparison of the QMC estimate with estimates from the original scaling hypothesis and its extended form. Symbols are individual iPEPS simulations with $D = (5, 6, 7, 8)$ and selected χ from 17 up to 200 for $D = (5, 6, 7)$ and up to 147 for $D = 8$.

optimizations is roughly $\chi/D^2 \gtrsim 2$. For bond dimensions $D = (6, 7, 8)$, we perform optimizations reaching environment dimensions χ up to 252, 196, and 160, respectively. The technical limitations are set by the memory requirements of the intermediate steps in the construction of all RDMs needed to compute observables.

The resulting fixed- (D, χ) iPEPS data at $D = (5, 6, 7, 8)$ for magnetization (energy) can no longer be described by the simple scaling ansatz $m^2 = m_0^2 + a/\xi + O(1/\xi^2)$ [$e = e_0 + c/\xi^3 + O(1/\xi^4)$], at least in the regime accessible by our simulations. In contrast to the AFM Heisenberg point, where the optimized ansatz reaches correlation lengths as large as $1/\xi \approx 0.125$, at $(J_2, J_3) = (0, 0.35)$ the largest correlation lengths attained are only $1/\xi \approx 0.3$. We believe this is a manifestation of frustration, where an equally good description of systems on patches of characteristic size ξ requires increasingly larger D and χ compared to the unfrustrated case. In order to extract thermodynamic estimates for magnetization and energy from our iPEPS data, we thus adopt an empirical approach following the idea behind an improved fit of magnetization at the AFM Heisenberg point. We postulate the following scaling hypotheses for magnetization and energy of an optimal iPEPS ansatz as functions of both correlation length and bond dimension D ,

$$m^2 = m_0^2 + \frac{m_1^2}{D} + \frac{m_2^2}{D^2} + \frac{a}{\xi} + \frac{b}{D\xi} + O(1/\xi^2), \quad (\text{C3})$$

$$e = e_0 + \frac{e_1}{D} + \frac{e_2}{D^2} + \frac{c}{\xi^3} + \frac{d}{(D\xi^3)} + O(1/\xi^4). \quad (\text{C4})$$

The functional form of these surfaces is motivated by the evidence that a simple FCLS hypothesis for the Néel

phase (C1) works appreciably well even close to the paramagnetic phase [67]. Moreover, for sufficiently large bond dimensions, the finite- D effects should become irrelevant, and the simple scaling hypothesis is recovered. We fit these surfaces to the iPEPS data for magnetization and energy at $D = (5, 6, 7, 8)$ and show the finite- D cuts of the resulting surfaces in Figs. 15(a) and 16(a), respectively.

Our thermodynamic estimate for magnetization is $m^2(1/D \rightarrow 0, 1/\xi \rightarrow 0) = -0.004(4)$, which is compatible with the QSL phase at $(J_2, J_3) = (0, 0.35)$. Similarly, the energy per site is estimated as $e(1/D \rightarrow 0, 1/\xi \rightarrow 0) = -0.56956(2)$. The coefficients of the fitted surfaces are listed in Table V.

Let us remark that while the limit $1/D, 1/\xi \rightarrow 0$ is unambiguous, the limit of surfaces in Eqs. (C3) and (C4) with only $1/\xi \rightarrow 0$ for small finite D might be unphysical since the optimal iPEPS instead realize finite correlation lengths even for environment dimensions $\chi \rightarrow \infty$.

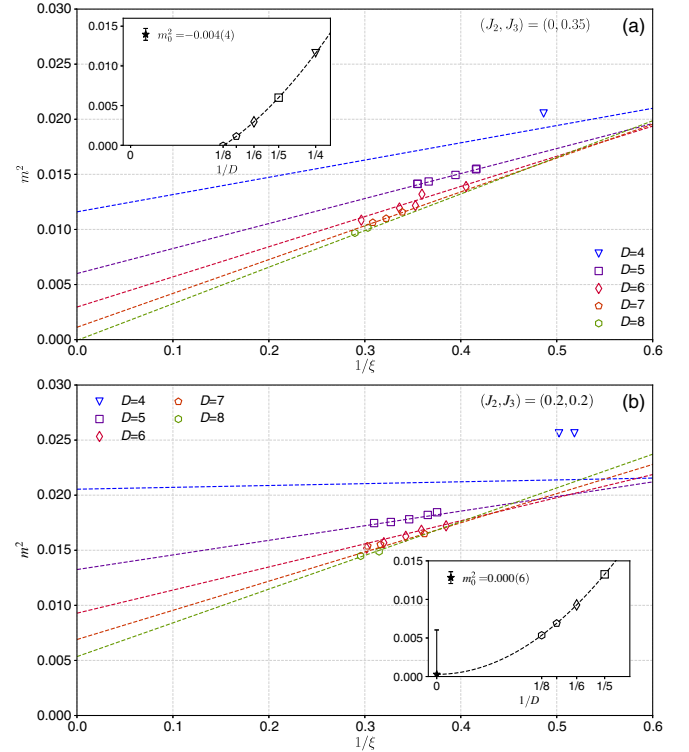


FIG. 15. Scaling of magnetization at $(J_2, J_3) = (0, 0.35)$ (a) and $(0.2, 0.2)$ (b). The colored dashed lines are fixed- D cuts of the surface $m^2(1/D, 1/\xi)$ obtained by a least-squares fit to Eq. (C3) ($D = 4$ is excluded from the fit). The colored symbols are iPEPS data for $D = (4, 5, 6, 7, 8)$ with environment dimensions χ up to 63, 151, 252, 196, and 160, respectively. In panel (b), an additional data point $(D, \chi) = (5, 300)$ is included. The inset shows the dashed $m^2(1/D)$ curve obtained in the limit $1/\xi \rightarrow 0$. The individual black points show a hypothetical value of m^2 reached in the limit of $1/\xi \rightarrow 0$ for $D = (4, 5, 6, 7, 8)$ (see text).

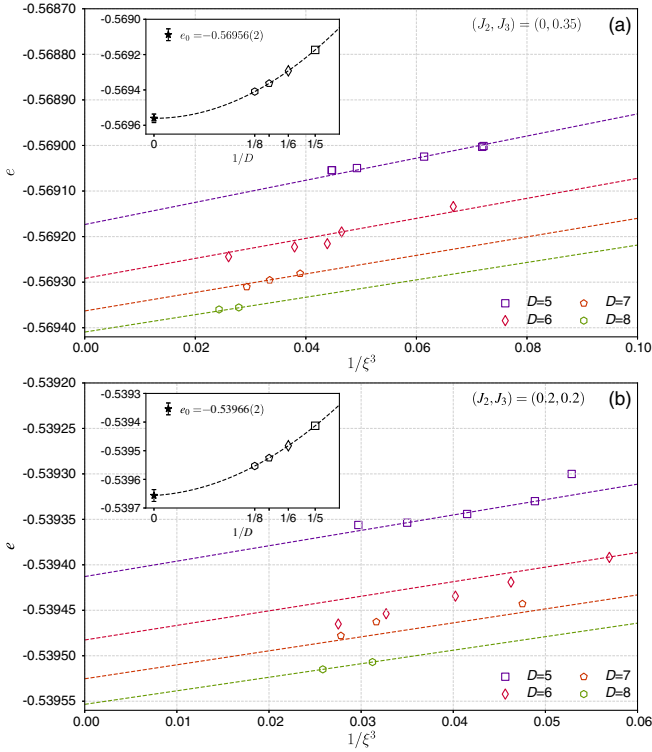


FIG. 16. Scaling of energy at $(J_2, J_3) = (0, 0.35)$ (a) and $(0.2, 0.2)$ (b). The colored dashed lines are fixed- D cuts (colored dashed lines) of the surface $e(1/D, 1/\xi)$ obtained by a least-squares fit to Eq. (C4). The colored symbols are iPEPS data for $D = (5, 6, 7, 8)$ with environment dimensions χ up to 151, 252, 196, and 160, respectively. In panel (b), an additional data point $(D, \chi) = (5, 300)$ is included. The inset shows the dashed $e(1/D)$ curve obtained in the limit $1/\xi \rightarrow 0$. The individual black points show a *hypothetical* value of e reached in the limit of $1/\xi \rightarrow 0$ for $D = (5, 6, 7, 8)$ (see text).

c. Point $(J_2, J_3) = (0.2, 0.2)$

The final point subjected to iPEPS analysis is the highly frustrated point $(J_2, J_3) = (0.2, 0.2)$ where both next-nearest neighbor and next-next-nearest-neighbor coupling play a role. As in the case of $(J_2, J_3) = (0, 0.35)$, we find that for bond dimensions $D = (6, 7, 8)$, well-behaved optimizations require environment dimensions of at least $\chi/D^2 \gtrsim 2$. The surface fits, as shown in Figs. 15(b) and 16(b), lead to thermodynamic estimates for magnetization $m^2(1/D \rightarrow 0, 1/\xi \rightarrow 0) = 0.000(6)$, compatible with the SL phase at $(J_2, J_3) = (0.2, 0.2)$, and the energy per site $e(1/D \rightarrow 0, 1/\xi \rightarrow 0) = -0.53966(2)$. The coefficients of the fitted surfaces are listed in Table V. The error on the m^2 estimate remains large and is mainly due to the limited range of correlation lengths we could reach for the computationally accessible bond and environment dimensions D, χ .

2. Comparison with finite PEPS results

Finally, we give a detailed comparison of the iPEPS and finite PEPS results within the QSL phase. As shown

TABLE V. Least-squares fits of scaling hypotheses for magnetization and energy, defined in Eqs. (C3) and (C4) for the (J_2, J_3) points we study. For each coefficient, the top number is the estimated value and the bottom number is the error on the estimate based on the covariance matrix obtained from the Jacobian of the least-squares cost function. The coefficient m_1^2 (e_1) is bound to be positive.

(J_2, J_3)	m_0^2	m_1^2	m_2^2	a	b
$(0, 0)$	0.09 467 0.00 021	0.03 642 0.00 192	-0.01 678 0.00 789
$(0, 0.35)$	-0.00 396 0.00 391	0.00 004 0.03 279	0.24 876 0.16 913	0.05 077 0.02 061	-0.14 044 0.11 525
$(0.2, 0.2)$	0.00 028 0.00 576	0 0.04 222	0.32 416 0.13 837	0.05 955 0.02 129	-0.23 147 0.12 325
	e_0	e_1	e_2	c	d
$(0, 0.35)$	-0.569561 0.00 024	0 0.00 307	0.00 968 0.00 212	0.00 104 0.00 198	0.00 691 0.01 079
$(0.2, 0.2)$	-0.539656 0.00 021	0.00 168 0.00 037	0.00 525 0.00 083	0.00 115 0.00 053	0.00 273 0.00 325

in Fig. 17, the PEPS energy (per site) computed on open $L \times L$ clusters shows finite-size effects significantly larger than the finite- ξ effects of the iPEPS data—as seen, e.g., from a simple comparison of the energy scales used in Figs. 16 and 17. This is due to the fact that the leading correction of the iPEPS energy goes as $1/\xi^3$ while the leading finite PEPS correction goes as $1/L$. However, the finite PEPS energy follows a very precise quadratic scaling in the inverse bulk size $1/\tilde{L}$, for a given choice of central bulk $\tilde{L} \times \tilde{L}$, enabling very precise fits and an accurate extrapolation to the thermodynamic limit. We observe a very good agreement between the iPEPS and PEPS extrapolated energies with up to 4 significant digits.

We have also compared the iPEPS connected spin-spin and dimer-dimer correlations to the ones obtained on finite strips. The generic connected spin-spin correlation function is $(-1)^r \langle \mathbf{S}_i \cdot \mathbf{S}_{i+r} \rangle - m_0^2$ for magnetic and non-magnetic phases, where m_0 is the thermodynamic limit AFM order, which would give precise decay behavior of spin correlations when the system size L is sufficiently large. In the QSL phase, the thermodynamic limit AFM order is 0, and the connected spin-spin correlation is $(-1)^r \langle \mathbf{S}_i \cdot \mathbf{S}_{i+r} \rangle$ for finite size calculations. For iPEPS, the finite D ($D = 8$ here) shows a residual staggered magnetization m_0 , and the connected spin-spin correlation function is $(-1)^r \langle \mathbf{S}_i \cdot \mathbf{S}_{i+r} \rangle - m_0^2$, which could provide a systematically improved description for the decay behavior of the QSL phase and would be exact in the limit

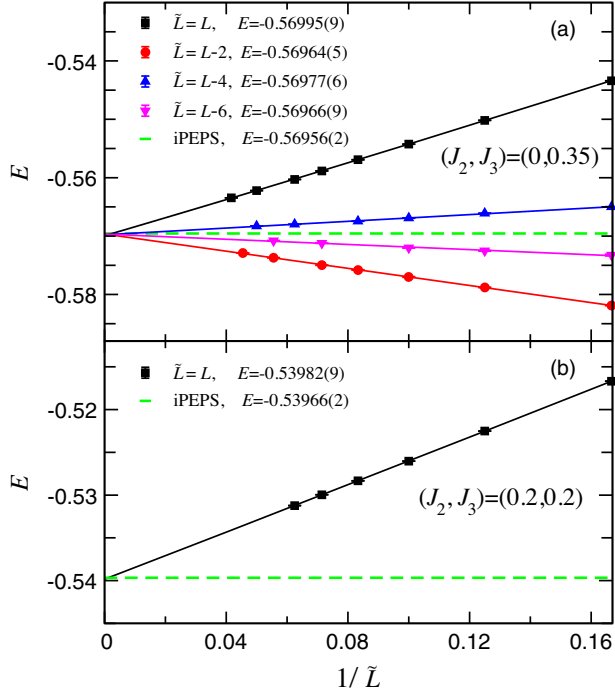


FIG. 17. Energy comparison between finite PEPS and iPEPS. Finite PEPS results on different system sizes are from $D = 8$, and iPEPS results (dashed lines) are from finite correlation scaling. (a) Finite-size scaling of different system sizes $L \times L$ up to $L = 24$ at $(J_2, J_3) = (0, 0.35)$. Energies from different bulk choices $\tilde{L} \times \tilde{L}$ are shown for extrapolations. Second-order extrapolations for $\tilde{L} = L$ or linear fittings for other cases are shown. Extrapolated energies of second-order fittings (not shown) for the $\tilde{L} = L - 2$ and $\tilde{L} = L - 4$ cases are $-0.5695(1)$ and $-0.5697(2)$, respectively. (b) Second-order extrapolations of energies at $(J_2, J_3) = (0.2, 0.2)$. The corresponding iPEPS and extrapolated finite PEPS energies are given in the legend.

$D \rightarrow \infty$ with a vanishing magnetic order. The finite PEPS and iPEPS spin-spin correlations are compared in Figs. 18(a), 18(c), and 18(e), showing good agreement and likely algebraic decays with similar exponents. We have also performed a similar comparison for the (staggered) dimer-dimer correlation function defined in Eq. (B1). Figures 18(b), 18(d), and 18(f) show the absolute value $|C_d(r)|$ vs r and again reveal good agreement between finite PEPS and iPEPS data, with similar algebraic decays. We point out that the likely algebraic decays of spin and dimer correlation functions at $(J_2, J_3) = (-0.4, 0.55)$ support that this point is critical, as suggested in Sec. II of the main text. However, we note that the correlations shown here are still subject to small finite L or finite D corrections. We observe that for increasing L/D , the correlations decay less rapidly, so the exponents extracted here (see values on the plots) can be considered as upper bounds of the true exponents (see Fig. 13 for more accurate values obtained from order parameter scaling).

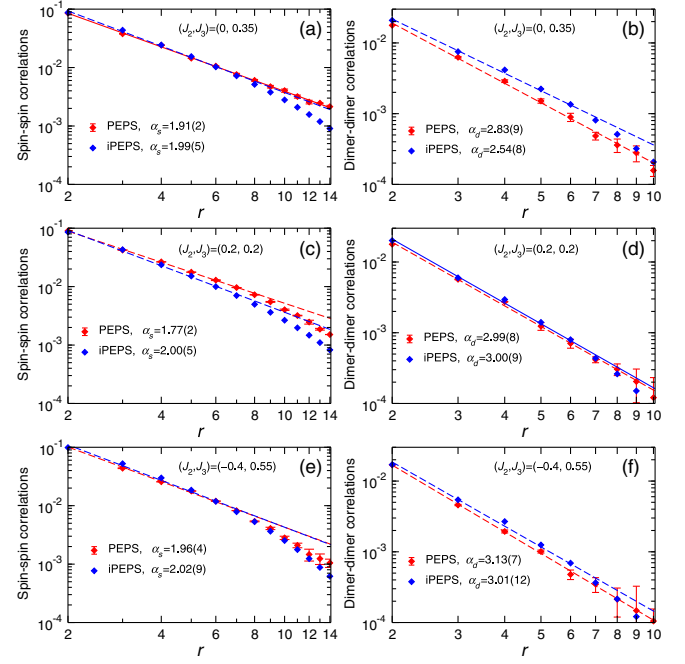


FIG. 18. Comparison between finite PEPS and iPEPS correlations at $D = 8$ (optimized as $\chi_{\text{opt}} = 160$ and evaluated at $\chi = 400$), plotted on a semilog scale. In the case of the finite PEPS correlations, a 20×28 strip is used at $(J_2, J_3) = (0, 0.35)$ and a 12×28 strip at $(J_2, J_3) = (0.2, 0.2)$ and $(J_2, J_3) = (-0.4, 0.55)$. Dashed lines are power-law fits using data up to intermediate distances $r \leq 7$.

- [1] Leon Balents, *Spin Liquids in Frustrated Magnets*, *Nature (London)* **464**, 199 (2010).
- [2] P. W. Anderson, *The Resonating Valence Bond State in La_2CuO_4 and Superconductivity*, *Science* **235**, 1196 (1987).
- [3] T. Senthil, Ashvin Vishwanath, Leon Balents, Subir Sachdev, and Matthew P. A. Fisher, *Deconfined Quantum Critical Points*, *Science* **303**, 1490 (2004).
- [4] T. Senthil, Leon Balents, Subir Sachdev, Ashvin Vishwanath, and Matthew P. A. Fisher, *Quantum Criticality Beyond the Landau-Ginzburg-Wilson Paradigm*, *Phys. Rev. B* **70**, 144407 (2004).
- [5] Anders W. Sandvik, *Evidence for Deconfined Quantum Criticality in a Two-Dimensional Heisenberg Model with Four-Spin Interactions*, *Phys. Rev. Lett.* **98**, 227202 (2007).
- [6] Adam Nahum, P. Serna, J. T. Chalker, M. Ortuño, and A. M. Somoza, *Emergent $\text{SO}(5)$ Symmetry at the Néel to Valence-Bond-Solid Transition*, *Phys. Rev. Lett.* **115**, 267203 (2015).
- [7] G. J. Sreejith, Stephen Powell, and Adam Nahum, *Emergent $\text{SO}(5)$ Symmetry at the Columnar Ordering Transition in the Classical Cubic Dimer Model*, *Phys. Rev. Lett.* **122**, 080601 (2019).
- [8] Roger G. Melko and Ribhu K. Kaul, *Scaling in the Fan of an Unconventional Quantum Critical Point*, *Phys. Rev. Lett.* **100**, 017203 (2008).

- [9] F.-J. Jiang, M. Nyfeler, S. Chandrasekharan, and U.-J. Wiese, *From an Antiferromagnet to a Valence Bond Solid: Evidence for a First-Order Phase Transition*, *J. Stat. Mech.* (2008) P02009.
- [10] Jie Lou, Anders W. Sandvik, and Naoki Kawashima, *Antiferromagnetic to Valence-Bond-Solid Transitions in Two-Dimensional $SU(n)$ Heisenberg Models with Multi-spin Interactions*, *Phys. Rev. B* **80**, 180414(R) (2009).
- [11] D. Charrier and F. Alet, *Phase Diagram of an Extended Classical Dimer Model*, *Phys. Rev. B* **82**, 014429 (2010).
- [12] Anders W. Sandvik, *Continuous Quantum Phase Transition between an Antiferromagnet and a Valence-Bond Solid in Two Dimensions: Evidence for Logarithmic Corrections to Scaling*, *Phys. Rev. Lett.* **104**, 177201 (2010).
- [13] Ribhu K. Kaul, *Quantum Criticality in $SU(3)$ and $SU(4)$ Antiferromagnets*, *Phys. Rev. B* **84**, 054407 (2011).
- [14] Matthew S. Block, Roger G. Melko, and Ribhu K. Kaul, *Fate of $\mathbb{C}P^{N-1}$ Fixed Points with q Monopoles*, *Phys. Rev. Lett.* **111**, 137202 (2013).
- [15] Kenji Harada, Takafumi Suzuki, Tsuyoshi Okubo, Haruhiko Matsuo, Jie Lou, Hiroshi Watanabe, Syngye Todo, and Naoki Kawashima, *Possibility of Deconfined Criticality in $SU(N)$ Heisenberg Models at Small N* , *Phys. Rev. B* **88**, 220408(R) (2013).
- [16] Kun Chen, Yuan Huang, Youjin Deng, A. B. Kuklov, N. V. Prokof'ev, and B. V. Svistunov, *Deconfined Criticality Flow in the Heisenberg Model with Ring-Exchange Interactions*, *Phys. Rev. Lett.* **110**, 185701 (2013).
- [17] Sumiran Pujari, Fabien Alet, and Kedar Damle, *Transitions to Valence-Bond Solid Order in a Honeycomb Lattice Antiferromagnet*, *Phys. Rev. B* **91**, 104411 (2015).
- [18] Adam Nahum, J. T. Chalker, P. Serna, M. Ortuño, and A. M. Somoza, *Deconfined Quantum Criticality, Scaling Violations, and Classical Loop Models*, *Phys. Rev. X* **5**, 041048 (2015).
- [19] Hui Shao, Wenan Guo, and Anders W. Sandvik, *Quantum Criticality with Two Length Scales*, *Science* **352**, 213 (2016).
- [20] F. F. Assaad and Tarun Grover, *Simple Fermionic Model of Deconfined Phases and Phase Transitions*, *Phys. Rev. X* **6**, 041049 (2016).
- [21] Toshihiro Sato, Martin Hohenadler, and Fakhre F. Assaad, *Dirac Fermions with Competing Orders: Non-Landau Transition with Emergent Symmetry*, *Phys. Rev. Lett.* **119**, 197203 (2017).
- [22] Yi-Zhuang You, Yin-Chen He, Cenke Xu, and Ashvin Vishwanath, *Symmetric Fermion Mass Generation as Deconfined Quantum Criticality*, *Phys. Rev. X* **8**, 011026 (2018).
- [23] Xue-Feng Zhang, Yin-Chen He, Sebastian Eggert, Roderich Moessner, and Frank Pollmann, *Continuous Easy-Plane Deconfined Phase Transition on the Kagome Lattice*, *Phys. Rev. Lett.* **120**, 115702 (2018).
- [24] Y. Liu, Z. Wang, T. Sato, M. Hohenadler, C. Wang, W. Guo, and F. F. Assaad, *Superconductivity from the Condensation of Topological Defects in a Quantum Spin-Hall Insulator*, *Nat. Commun.* **10**, 2658 (2019).
- [25] Chong Wang, Adam Nahum, Max A. Metlitski, Cenke Xu, and T. Senthil, *Deconfined Quantum Critical Points: Symmetries and Dualities*, *Phys. Rev. X* **7**, 031051 (2017).
- [26] V. Gorbenko, S. Rychkov, and B. Zan, *Walking, Weak First-Order Transitions, and Complex CFTs*, *J. High Energy Phys.* **10** (2018) 108.
- [27] Victor Gorbenko, Slava Rychkov, and Bernardo Zan, *Walking, Weak First-Order Transitions, and Complex CFTs II. Two-Dimensional Potts Model at $Q > 4$* , *SciPost Phys.* **5**, 50 (2018).
- [28] Li Zhijin, *Solving QED₃ with Conformal Bootstrap*, arXiv: 2018.09281.
- [29] Jong Yeon Lee, Yi-Zhuang You, Subir Sachdev, and Ashvin Vishwanath, *Signatures of a Deconfined Phase Transition on the Shastry-Sutherland Lattice: Applications to Quantum Critical SrCu₂(BO₃)₂*, *Phys. Rev. X* **9**, 041037 (2019).
- [30] Ruochen Ma and Chong Wang, *Theory of Deconfined Pseudocriticality*, *Phys. Rev. B* **102**, 020407(R) (2020).
- [31] Adam Nahum, *Note on Wess-Zumino-Witten Models and Quasiuniversality in 2 + 1 Dimensions*, *Phys. Rev. B* **102**, 201116(R) (2020).
- [32] Bowen Zhao, Jun Takahashi, and Anders W. Sandvik, *Multicritical Deconfined Quantum Criticality and Lifshitz Point of a Helical Valence-Bond Phase*, *Phys. Rev. Lett.* **125**, 257204 (2020).
- [33] Yin-Chen He, Junchen Rong, and Ning Su, *Non-Wilson-Fisher Kinks of $O(N)$ Numerical Bootstrap: From the Deconfined Phase Transition to a Putative New Family of CFTs*, *SciPost Phys.* **10**, 115 (2021).
- [34] Zhenjiu Wang, Michael P. Zaletel, Roger S. K. Mong, and Fakhre F. Assaad, *Phases of the (2 + 1) Dimensional $SO(5)$ Nonlinear Sigma Model with Topological Term*, *Phys. Rev. Lett.* **126**, 045701 (2021).
- [35] Jianwei Yang, Anders W. Sandvik, and Ling Wang, *Quantum Criticality and Spin Liquid Phase in the Shastry-Sutherland Model*, *Phys. Rev. B* **105**, L060409 (2022).
- [36] Wen-Yuan Liu, Shou-Shu Gong, Yu-Bin Li, Didier Poilblanc, Wei-Qiang Chen, and Zheng-Cheng Gu, *Gapless Quantum Spin Liquid and Global Phase Diagram of the Spin-1/2 $J_1 - J_2$ Square Antiferromagnetic Heisenberg Model*, *Science bulletin* **67**, 1034 (2022).
- [37] E. Rastelli, L. Reatto, and A. Tassi, *Quantum Fluctuations and Phase Diagram of Heisenberg Models with Competing Interactions*, *J. Phys. C* **19**, 6623 (1986).
- [38] P. Chandra and B. Doucot, *Possible Spin-Liquid State at Large S for the Frustrated Square Heisenberg Lattice*, *Phys. Rev. B* **38**, 9335 (1988).
- [39] L. B. Ioffe and A. I. Larkin, *Effective Action of a Two-Dimensional Antiferromagnet*, *Int. J. Mod. Phys. B* **02**, 203 (1988).
- [40] F. Figueirido, A. Karlhede, S. Kivelson, S. Sondhi, M. Rocek, and D. S. Rokhsar, *Exact Diagonalization of Finite Frustrated Spin-(1/2) Heisenberg Models*, *Phys. Rev. B* **41**, 4619 (1990).
- [41] N. Read and Subir Sachdev, *Large N Expansion for Frustrated Quantum Antiferromagnets*, *Phys. Rev. Lett.* **66**, 1773 (1991).
- [42] E. Rastelli and A. Tassi, *Nonlinear Effects in the Spin-Liquid Phase*, *Phys. Rev. B* **46**, 10793 (1992).
- [43] Jaime Ferrer, *Spin-Liquid Phase for the Frustrated Quantum Heisenberg Antiferromagnet on a Square Lattice*, *Phys. Rev. B* **47**, 8769 (1993).

- [44] P. W. Leung and Ngar-wing Lam, *Numerical Evidence for the Spin-Peierls State in the Frustrated Quantum Antiferromagnet*, *Phys. Rev. B* **53**, 2213 (1996).
- [45] Luca Capriotti, Douglas J. Scalapino, and Steven R. White, *Spin-Liquid versus Dimerized Ground States in a Frustrated Heisenberg Antiferromagnet*, *Phys. Rev. Lett.* **93**, 177004 (2004).
- [46] Luca Capriotti and Subir Sachdev, *Low-Temperature Broken-Symmetry Phases of Spiral Antiferromagnets*, *Phys. Rev. Lett.* **93**, 257206 (2004).
- [47] Matthieu Mambri, Andreas Läuchli, Didier Poilblanc, and Frédéric Mila, *Plaquette Valence-Bond Crystal in the Frustrated Heisenberg Quantum Antiferromagnet on the Square Lattice*, *Phys. Rev. B* **74**, 144422 (2006).
- [48] Philippe Sindzingre, Nic Shannon, and Tsutomu Momoi, *Phase Diagram of the Spin-1/2 J_1 - J_2 - J_3 Heisenberg Model on the Square Lattice*, *J. Phys. Conf. Ser.* **200**, 022058 (2010).
- [49] Bowen Zhao, Jun Takahashi, and Anders W. Sandvik, *Comment on Gapless Spin Liquid Ground State of the Spin-1/2 J_1 - J_2 Heisenberg Model on Square Lattices*, *Phys. Rev. B* **101**, 157101 (2020).
- [50] Anders W. Sandvik, *Computational Studies of Quantum Spin Systems*, *AIP Conf. Proc.* **1297**, 135 (2010).
- [51] Muwei Wu, Shou-Shu Gong, Dao-Xin Yao, and Han-Qing Wu, *Phase Diagram and Magnetic Excitation of J_1 - J_3 Heisenberg Model on the Square Lattice*, [arXiv:2022.07910](https://arxiv.org/abs/2022.07910).
- [52] Xiao Yan Xu, Yang Qi, Long Zhang, Fakher F. Assaad, Cenke Xu, and Zi Yang Meng, *Monte Carlo Study of Lattice Compact Quantum Electrodynamics with Fermionic Matter: The Parent State of Quantum Phases*, *Phys. Rev. X* **9**, 021022 (2019).
- [53] Lukas Janssen, Wei Wang, Michael M. Scherer, Zi Yang Meng, and Xiao Yan Xu, *Confinement Transition in the QED₃-Gross-Neveu-XY Universality Class*, *Phys. Rev. B* **101**, 235118 (2020).
- [54] Henry Shackleton, Alex Thomson, and Subir Sachdev, *Deconfined Criticality and a Gapless Z_2 Spin Liquid in the Square-Lattice Antiferromagnet*, *Phys. Rev. B* **104**, 045110 (2021).
- [55] Xiao-Gang Wen, *Quantum Orders and Symmetric Spin Liquids*, *Phys. Rev. B* **65**, 165113 (2002).
- [56] Francesco Ferrari and Federico Becca, *Gapless Spin Liquid and Valence-Bond Solid in the J_1 - J_2 Heisenberg Model on the Square Lattice: Insights from Singlet and Triplet Excitations*, *Phys. Rev. B* **102**, 014417 (2020).
- [57] S. Ebadi, T. T. Wang, H. Levine *et al.*, *Quantum Phases of Matter on a 256-Atom Programmable Quantum Simulator*, *Nature (London)* **595**, 227 (2021).
- [58] P. Scholl, M. Schuler, H. J. Williams *et al.*, *Quantum Simulation of 2D Antiferromagnets with Hundreds of Rydberg Atoms*, *Nature (London)* **595**, 233 (2021).
- [59] G. Semeghini, H. Levine, A. Keesling, S. Ebadi *et al.*, *Probing Topological Spin Liquids on a Programmable Quantum Simulator*, *Science* **374**, 1242 (2021).
- [60] F. Verstraete, V. Murg, and J. I. Cirac, *Matrix Product States, Projected Entangled Pair States, and Variational Renormalization Group Methods for Quantum Spin Systems*, *Adv. Phys.* **57**, 143 (2008).
- [61] I. P. McCulloch and M. Gulácsi, *The Non-Abelian Density Matrix Renormalization Group Algorithm*, *Europhys. Lett.* **57**, 852 (2002).
- [62] Wen-Yuan Liu, Shao-Jun Dong, Yong-Jian Han, Guang-Can Guo, and Lixin He, *Gradient Optimization of Finite Projected Entangled Pair States*, *Phys. Rev. B* **95**, 195154 (2017).
- [63] Wen-Yuan Liu, Yi-Zhen Huang, Shou-Shu Gong, and Zheng-Cheng Gu, *Accurate Simulation for Finite Projected Entangled Pair States in Two Dimensions*, *Phys. Rev. B* **103**, 235155 (2021).
- [64] A. W. Sandvik and G. Vidal, *Variational Quantum Monte Carlo Simulations with Tensor-Network States*, *Phys. Rev. Lett.* **99**, 220602 (2007).
- [65] Norbert Schuch, Michael M. Wolf, Frank Verstraete, and J. Ignacio Cirac, *Simulation of Quantum Many-Body Systems with Strings of Operators and Monte Carlo Tensor Contractions*, *Phys. Rev. Lett.* **100**, 040501 (2008).
- [66] H. C. Jiang, Z. Y. Weng, and T. Xiang, *Accurate Determination of Tensor Network State of Quantum Lattice Models in Two Dimensions*, *Phys. Rev. Lett.* **101**, 090603 (2008).
- [67] Juraj Hasik, Didier Poilblanc, and Federico Becca, *Investigation of the Néel Phase of the Frustrated Heisenberg Antiferromagnet by Differentiable Symmetric Tensor Networks*, *SciPost Phys.* **10**, 12 (2021).
- [68] J. Hasik and G. B. Mbeng, *PEPS-Torch: A Differentiable Tensor Network Library for Two-Dimensional Lattice Models* (2020), <https://github.com/jurajHasik/peps-torch>.
- [69] Philippe Corboz, Piotr Czarnik, Geert Kapteijns, and Luca Tagliacozzo, *Finite Correlation Length Scaling with Infinite Projected Entangled-Pair States*, *Phys. Rev. X* **8**, 031031 (2018).
- [70] Michael Rader and Andreas M. Läuchli, *Finite Correlation Length Scaling in Lorentz-Invariant Gapless iPEPS Wave Functions*, *Phys. Rev. X* **8**, 031030 (2018).
- [71] Bram Vanhecke, Juraj Hasik, Frank Verstraete, and Laurens Vanderstraeten, *A Scaling Hypothesis for Projected Entangled-Pair States*, [arXiv:2102.03143](https://arxiv.org/abs/2102.03143).